

University of Nevada, Reno

**Tunable Reversible Dry Adhesion of Elastomeric Post Enabled
by Stiffness Tuning of Microfluidic LMPA Thin Film**

A thesis submitted in partial fulfillment for
the degree of Master of Science in
Mechanical Engineering

By

Patrick R. Stampfli

Dr. Wanliang Shan/Thesis Advisor

December 2017

Copyright by Patrick R. Stampfli 2017

All Rights Reserved



THE GRADUATE SCHOOL

We recommend that the thesis
prepared under our supervision by

PATRICK R. STAMPFLI

Entitled

**Tunable Reversible Dry Adhesion of Elastomeric Post Enabled by Stiffness Tuning
of Microfluidic LMPA Thin Film**

be accepted in partial fulfillment of the
requirements for the degree of

MASTER OF SCIENCE

Wanliang Shan, Ph. D., Advisor

Matteo Aureli, Ph. D., Committee Member

Jeffrey LaCombe, Ph. D., Graduate School Representative

David W. Zeh, Ph.D., Dean, Graduate School

December, 2017

ABSTRACT

The goal of this study is to investigate the effects and underlying mechanisms of stiffness tuning on tunable reversible dry adhesion of an elastomeric post. This research introduces a novel device constructed out of a soft elastomer, polydimethylsiloxane (PDMS), with micro channels injected with low melting point alloy (LMPA) that can soften by applying a voltage. In contrast to traditional handling devices, such as metallic robot handlers, this soft gripper enables compliant manipulation of delicate fragile objects such as a thin glass slide. In this thesis, the design and fabrication of the elastomeric posts and the effects of three adhesion testing conditions will be presented. The first testing condition provided the baseline adhesion values that would be later referenced to certify adhesion reversibility. The second condition demonstrates the device's ability to change adhesion forces on the spot, or dynamically. The third condition displays the ability of the device to maintain this adhesion change when activated and deactivated repeatedly. Theoretical Finite Element modeling provides insights indicating a maximum adhesion when varying one critical geometrical parameter, which was later confirmed with experiments. Experimental results prove the device's capability of dynamically tunable reversible dry adhesion. This novel approach to tunable dry adhesion exhibits the feasibility of soft grippers that would not require complicated systems for activation but instead only need low power and simple circuitry, and thus have potential to function as effective soft gripping devices.

ACKNOWLEDGEMENTS

Thank you, Dr. Wanliang Shan, my thesis advisor, for the guidance to complete this project. Dr. Emil Geiger, thank you for the opportunity to progress my education.

To my parents, Robert and Deborah, and grandparents, George and Norma, thank you for the endless support throughout my education.

I would like to thank Mr. Amir Mohammadi Nasab for his efforts during the project. His expertise was essential to the design, theoretical modeling, and testing for this research project.

I am grateful to my committee members, Dr. Matteo Aureli and Dr. Jeffrey LaCombe, for reviewing my work and providing excellent feedback.

To my grandfather, Jack Stooksberry, thank you for inspiring me to always keep learning.

I would like to give my sincerest gratitude to Mr. Amit Saini for his support and friendship throughout my college education.

I give special thanks to the members of the Shan Research Group for being friendly and supportive colleagues.

Table of Contents

<i>ABSTRACT</i>	<i>i</i>
<i>ACKNOWLEDGEMENTS</i>	<i>ii</i>
<i>LIST OF TABLES</i>	<i>v</i>
<i>LIST OF FIGURES</i>	<i>vi</i>
Chapter 1 – Introduction	1
1.1 Introduction	1
1.2 Soft Robotic Grippers	1
1.3 MEMS Handling	6
1.4 Bio-inspired Adhesives.....	10
Chapter 2 – Background	17
2.1 Introduction	17
2.2 Tunable Adhesion.....	17
2.3 Theory	25
2.4 Project.....	33
Chapter 3 – Design and Fabrication	34
3.1 Introduction	34
3.2 Design	34
3.3 Fabrication Methods.....	39
Chapter 4 – Testing Method and Setup.....	46
4.1 Introduction	46
4.2 Experimental Setup	46
4.3 Testing Issues	49
4.4 Testing Conditions	52
Chapter 5 – Results and Discussion	55
Introduction	55
5.1 Simulation Results.....	55
5.2 Experimental Results	60
5.3 Discussion.....	65
Chapter 6 – Summary, Conclusions, and Future Work.....	67
6.1 Summary	67

<i>6.2 Conclusions</i>	68
<i>6.3 Future Work</i>	69
References	71

LIST OF TABLES

No table of figures entries found.

LIST OF FIGURES

Figure 1-1: (a) Schematic of the soft gripper and the different layers. (b) The gripper in the resting state with the fingers curled outwards, voltage is applied causing the fingers to curl inward and conforming to the egg (60.9 g) for pick up. (c) Gripper picking up a thin membrane water balloon (35.6 g). (d) Picking up a piece of paper (0.8 g). (e) Teflon tube (80.8 g). (f) Metallic oil can (82.1 g) [8].	3
Figure 1-2: Images of the versatile adaptable soft gripper developed by the Shan Research Group at the University of Nevada, Reno (a) ping pong ball (b) roll of tape (c) marble (d) small clamp (e) binder clip (f) petri dish (g) empty box (h) With the tunable rigidity ligaments the gripper can twist resulting in the rotation of the object that is picked up. [9].	4
Figure 1-3: Shows the gripper's ability to pick up a variety of objects. (a) Tupperware (b) model of a human hand (c) cactus (d) screw (e) pen (f) keys (g) a compact disc (h) egg (i) bag of milk [11].	5
Figure 1-4: (a) The process flow for picking up and placing of an object with the stamp. (b) The stamp in a low adhesion state. (c) The same stamp in a high adhesion state. (d) Stamp with a dimple in the middle in a low adhesion state. (e) The dimple retracted results in a high adhesion state [22].	7
Figure 1-5: Schematic showing the multiple die pick up capabilities of the conical SMP stamp array and the use of a laser for localized heating, resulting in selective placement [23].	8
Figure 1-6: Process flow of shear transfer printing. An elastomeric stamp is brought into contact with the target which is then picked up and transported to the desired area. Once in position, the target is placed down and shear is slowly applied allowing the stamp to disengage resulting in placement of the target [25].	9
Figure 1-7: Schematic of a multi-roller transfer printing process [27].	9

Figure 1-8: Left: shows the bottom of a gecko’s foot. Right: the hierarchy of hairs called spatula that aid in the gecko’s ability to climb multiple surfaces [32].	10
Figure 1-9: (a) SEM image of a gecko toe pad displaying the hierarchy of structure. (b) Fabrication process overview. (c) Polymer pillars with carbon nanotubes on the tips. (d) Magnification of the carbon nanotube tips [36].	11
Figure 1-10: (a) Toe pad of a gecko displaying the lamellar arrays courtesy of Professor Kellar Autumn. (b) The fabricated device with similar lamellar arrays. (c, d) SEM imagery of the nanofiber arrays on lamellar flaps [37].	12
Figure 1-11: Octopus inspired film with “suckers”. When the hydrogel is heated, expansion of the inner chamber pulls a vacuum for suction to a surface. Then, cooling causes the hydrogel to swell decreasing the internal volume and releasing the vacuum and object. [38].	13
Figure 1-12: A gecko-inspired wall climbing robot with fibrillar adhesive pads on the feet. Actuators on the toes allow for an upwards toe peeling motion similar to a gecko [43].	14
Figure 1-13: Wheel-like robot with mushroom tip fibrillar arrays on the pads [44].	14
Figure 1-14: Tank-like wall climbing robot with bio-inspired adhesive treads scaling a vertical surface [45].	15
Figure 1-15: Three frames of a video showing a 70kg climber scaling a vertical wall with the gecko-inspired adhesion system [46].	15
Figure 2-1: (a) Nickel cantilever with polymer nano-rods on the surface. (b) Magnification of a gecko foot setae branch with spatulae at the end. (c) Polymer nano-rod coated nickel cantilever array displaying hierarchical mimicry when compared to (d) a setae array of a gecko foot. Right: Top shows the cantilevers under no magnetic field exposing the polymer nano-rods in an adhesion “ON” state. Bottom shows the introduction of a magnetic field resulting in the cantilevers rotating and covering the nano-rods in an adhesive “OFF” state [49].	18

Figure 2-2: Schematic showing the test setup for the reversible switchable adhesion device. Heat is applied allowing the liquid Gallium to conform to the desired surface. The system is then cooled to solidify the Gallium resulting in temporary adhesion. When adhesion is no longer required heat is then applied liquefying the Gallium and releasing the bond between the elastomer post and the surface [50].	19
Figure 2-3: Shows the test set up for the step-like micro pillars. The system can move in the x direction allowing for the user to define the direction of drag to obtain the desired increase or decrease in adhesion [51].	20
Figure 2-4: Shows how the step-like post reacts to the drag direction. By dragging to the left a reduction in contact surface area occurs resulting in reduced adhesion. By dragging to the right an increase in contact surface area occurs resulting in increased adhesion [51].	20
Figure 2-5: Schematic of the adhesion process starting with a cooled micro SMP array. Heat is then applied along with a preload to deform the wedges resulting in a high adhesion state. To maintain this state, the array is cooled causing the wedges to remain deformed for high adhesion allowing the target object to be manipulated [52].	21
Figure 2-6: Left: The film in an adhesion off state due to the posts making a point contact because of surface wrinkling. Right: The film in an adhesion on state. Stretching the film allows the posts to make a surface contact increasing adhesion [53].	22
Figure 2-7: (a) Elastomer post with rigid core diagram (b) PDMS post without a rigid core (c) PDMS post with a PEEK core [54].	23
Figure 2-8: An elastomer post with a tunable cPBE core. Normally the core is rigid and upon activation by applying a voltage, the core becomes soft allowing the sample to stretch.	24
Figure 2-9: The schematic of the combined tunable core (Black) and variable stiffness interfacial heater (Purple) injected with LMPA (White). This device allows for multi-level dynamic tuning of dry adhesion. [55].	24

Figure 2-10: The three Fracture Modes associated with crack growth Tension, Sliding Shear, and Scissoring Shear [56].	26
Figure 2-11: Experimental data for a specific material and the increase in G_C that is required for crack growth as the sample experiences different modes [56].	26
Figure 2-12: The critical energy release rate for pure PDMS at different temperatures. [21]	28
Figure 2-13: Simulation of a 2D pure PDMS post under a 28 kPa tension load. Results show a maximum strain at the crack tip of 1.0203, resulting in a G equal to G_C meaning that the crack will propagate.	28
Figure 2-14: PDMS post with embedded rigid core subjected to the same 28 kPa tension load. Results show a more uniform strain distribution resulting in a lower maximum strain value of 0.2318 giving a G lower than G_C meaning that a higher load would need to be applied to propagate the crack.	29
Figure 2-15: Top: stress distribution of the pure PDMS post with a max stress of 1.0206 MPa. Bottom: More uniform stress distribution of the PDMS post with embedded rigid core with a max stress of 0.2141 MPa.	31
Figure 2-16: Top: Deformation of the pure PDMS post with a maximum displacement of 0.14415 mm. Bottom: Deformation of the PDMS post with rigid core having a maximum deformation of 0.011548 mm. By reducing the maximum displacement experienced by a sample, strain can be minimized thus keeping G lower for higher applied loads resulting in a change of dry adhesion.	32
Figure 2-17: PDMS main body with LMPA filled micro-channels.	33
Figure 3-1: Top: shows a similarly sealed liquid metal heater and the formation voids at high temperatures due to different thermal expansion coefficients of the PDMS and EGaIn. Bottom: shows a liquid metal heater that is exposed to a constant a flow of liquid metal, filling the voids as they form [58].	35

Figure 3-2: First version of the variable stiffness device. Channels were not close enough to the edges to allow the tunable plane to influence the system.	36
Figure 3-3: (a) Layout of the variable stiffness device. (b) Non-activated LMPA channels displaying rigid characteristics. (c) When activated, the LMPA goes through a phase change from solid to liquid allowing the device to bend. (d) Cross section of the device [59].	37
Figure 3-4: Bottom view of the final device design. LMPA channels were designed to be as close to each other and the edge as possible while maintaining device integrity for testing.	38
Figure 3-5: Cross sectional view of the main body with 200 μm wide channels where $L = 700 \mu\text{m}$, $H = 400 \mu\text{m}$, and V was varied from 200 to 1200 μm . Electrode wells have a conical shape to help keep material in the channel under compressive loading.	38
Figure 3-6: Left: Top view of the 3D printed mold. Right: Crosssectional view of the mold showing the top shelf feature added to ensure a clean removal of the part to preserve the bonding surface.	40
Figure 3-7: Left: 3D printed mold of micro channels. Right: De-gassing of the PDMS after casting is essential to ensure that no air bubbles are close to the channels.	41
Figure 3-8: Exploded view of the final device. The sealing layer was attached via corona discharge. After the bond between the sealing layer and the main body matured, the channels were injected with LMPA while also inserting the electrodes. The spacer block was then attached with uncured PDMS and left to cure. Once the PDMS was cured and the spacer block secured in place, the electrodes were threaded through the side of the spacer block and the sample was sealed with more uncured PDMS before being attached to the post with uncured PDMS.	44
Figure 3-9: Left: Front side view of sample. Right: Side view of sample.	45
Figure 4-1: The experimental setup used for all the testing. A 50 N load cell was installed for more precise measuring.	47

Figure 4-2: Close-up of the testing area showing exposed copper electrodes, fixed glass substrate, and fixture used to attach the post to the Instron.	48
Figure 4-3: Picture taken under the microscope of a clear breakage in the LMPA channel that results in an un-usable sample as it cannot be activated. This type of break was repairable.	49
Figure 4-4: Left to Right: an un-tested sample. Same sample after testing showing the voids formed that resulted in a loss of resistance. After the repair process was performed, a baseline test was performed to confirm the adhesion value remained the same after repair.	50
Figure 4-5: Images of breached sidewalls resulting in short circuiting of the sample. Areas within the red boxes are the spaces in between channels and should appear clear but instead are polluted with LMPA.	51
Figure 4-6: LMPA can be seen on the surface of the sample as a result of a failed sealing layer. Sealing layer thickness was roughly 100 μ m.	51
Figure 4-7: (1) Sample is brought into contact with glass surface. (2) Compressive preload of 14 N is held for 1 minute. (3) After 1 minute the tension is applied. (4) The sample loses contact with the glass surface concluding the test.	52
Figure 4-8: (1) Sample is brought into contact with glass surface. (2) Compressive preload of 14 N is applied for 1 minute with activation occurring in the last 30 seconds. (3) Tension is applied while the sample is still activated. (4) Sample loses contact with glass concluding the test.	53
Figure 4-9: (1) Sample is activated and brought into contact with the glass. (2) Compressive preload of 14 N applied for 1 min. (3) Sample is pulled away from the surface. (4) Sample loses contact with glass surface concluding the test.	54
Figure 5-1: The simulations conducted were of a 2D quarter model of a LMPA core sample. Variables of the simulation were the height of the LMPA channel, h, and the thickness of the sealing layer, t.	56

Figure 5-2: Shows the stress distributions for multiple LMPA layer and sealing layer thicknesses. Results show that for the tested system of $h=0.4\text{mm}$ the crack should begin on the edge. As the LMPA layer gets thicker, the crack location begins to move towards the center.	57
Figure 5-3: Results of the FEM simulations show that for the LMPA layer thickness of $400\mu\text{m}$, there should be a maximum adhesion value with a sealing layer thickness of $600\mu\text{m}$	59
Figure 5-4: Condition I results show a maximum baseline adhesion value associated with the $600\mu\text{m}$ sealing layer thickness as predicted by the FE simulation. Other data follows the behavioral trend but deviates possibly due to delamination effects. Error bars correlate to the standard deviation.	61
Figure 5-5: Condition II results show the same simulation trend with a maximum at $600\mu\text{m}$ sealing layer. One of the samples from the $400\mu\text{m}$ sealing layer thickness batch catastrophically failed during this test.....	62
Figure 5-6: Condition III was performed to investigate the effect an initial un-activated surface contact versus an activated initial surface contact. The resulting adhesions forces were slightly lower than those of an initial un-activated surface contact.	63
Figure 5-7: Comparing the adhesion change ratio of Condition I/Condition II and Condition I/Condition III.	64
Figure 5-8: Left to Right: frames taken from the demo video show the device holding the 4.46 N weight for approximately six seconds before the device is activated dropping the weight in less than two seconds. The multi-meter shows when the device was activated with 5.5 volts	65
Figure 5-9: Summary of the adhesion data for A and B samples. A maximum adhesion force seen at $600\mu\text{m}$ sealing layer thickness is consistent with FE simulations.....	66

Chapter 1 – Introduction

1.1 Introduction

This section will introduce some examples of soft robotic grippers, and their beneficial characteristics in regard to diverse repetitive processes and the wide range of geometric shapes and delicacies they can handle. The difficulties involved with the handling of Micro-Electro-Mechanical Systems (MEMS) either during fabrication or assembly will also be presented along with bio-mimicry films inspired by nature. A background on tunable adhesion and the theory will familiarize the readers with the concept before adventuring into the details of the research project.

1.2 Soft Robotic Grippers

In the dynamic world of high-tech industries, it is vital to create the tools necessary to handle various parts or devices either during highly repetitive tasks such as manufacturing, or everyday tasks involving human-machine interaction [1]. These tools, such as grippers, have proven themselves reliable, effective, and vital to some production processes [2, 3]. However, with traditional materials like metals, they do not allow for much adaptability or flexibility in regards to handling multiple or complex geometries, and objects varying in delicacy [4-7]. For example, when the dimension of a product changes, new tooling can be required to accommodate this change, and the process of re-tooling an entire manufacturing or assembly line can be time consuming and financially costly. The emerging research fields of Soft Robotics and Bio-Inspired Robotics aim to address this challenge by providing alternative solutions that involve adaptive grippers to

accommodate a plethora of geometries, weights, and materials to advance the capabilities and implementations of soft materials in large scale industrial manufacturing and assembly processes [2]. Among earlier attempts at providing these solutions, some grippers were sophisticated in design while others operated with relatively simple mechanisms and used innovative materials, thus reducing the burden of traditional metallic handling structures. For example, Jun Shintake et al. created a soft gripper that employs the phenomenon of electroadhesion and electrostatic actuation with integrated self-sensing that has the capabilities of manipulating objects varying in geometry, weight, and fragility [8]. In the resting state the fingers of the gripper curls outwards; when voltage is applied the fingers curl inwards conforming to the target object. When the object is to be placed back down the voltage is removed, causing the fingers to curl outwards releasing the object.

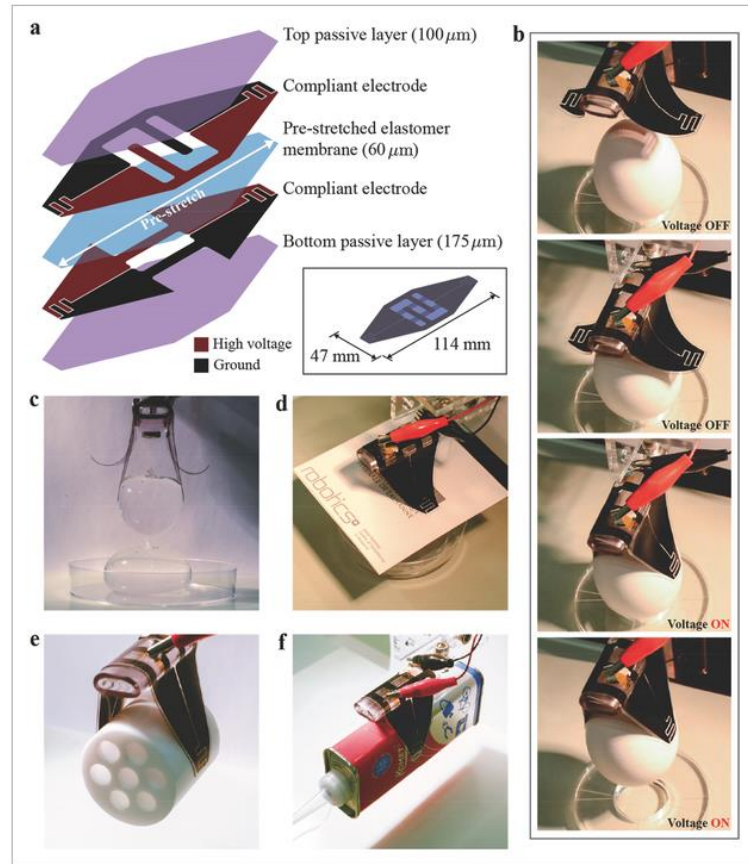


Figure 1-1: (a) Schematic of the soft gripper and the different layers. (b) The gripper in the resting state with the fingers curled outwards, voltage is applied causing the fingers to curl inward and conforming to the egg (60.9 g) for pick up. (c) Gripper picking up a thin membrane water balloon (35.6 g). (d) Picking up a piece of paper (0.8 g). (e) Teflon tube (80.8 g). (f) Metallic oil can (82.1 g) [8].

Development of soft smart materials increases the capabilities of soft grippers such as the one developed by A. M. Nasab et al. [9]. This gripper was outfitted with rigidity tunable elastomer strips as ligaments. The ligaments were developed by Shan et al. and are a conductive propylene-based elastomer (cPBE) embedded in a polydimethylsiloxane (PDMS) matrix [10]. The cPBE strips will soften when exposed to an electrical current resulting in tunable rigidity. The gripper, shown in Figure 1-2, is composed of three PDMS pressure chamber fingers that have EcoFlex ‘knuckles’ with each finger having

three cPBE strips as ligaments. By pressurizing the fingers and activating the ligaments with an electrical voltage, the user can dictate which way the fingers bend in real time. When the target object has been gripped and manipulated, it can be placed back down by depressurizing the fingers, and deactivating the cPBE strips to allow the structure to return to a neutral position.

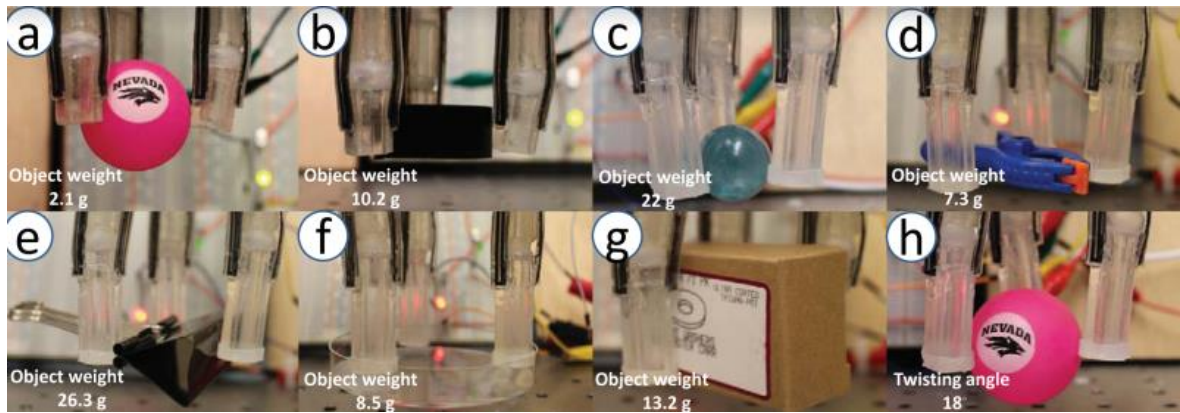


Figure 1-2: Images of the versatile adaptable soft gripper developed by the Shan Research Group at the University of Nevada, Reno (a) ping pong ball (b) roll of tape (c) marble (d) small clamp (e) binder clip (f) petri dish (g) empty box (h) With the tunable rigidity ligaments the gripper can twist resulting in the rotation of the object that is picked up. [9]

Hao et al. developed a four-finger soft gripper that can pick up a multitude of objects varying in size, weight, and geometry by utilizing pneumatics. Pressure chambers in the fingers are fabricated such that when a vacuum is pulled the fingers curl outwards, and oppositely, when the chambers are pressurized the fingers curl inwards conforming to the target object for pickup.

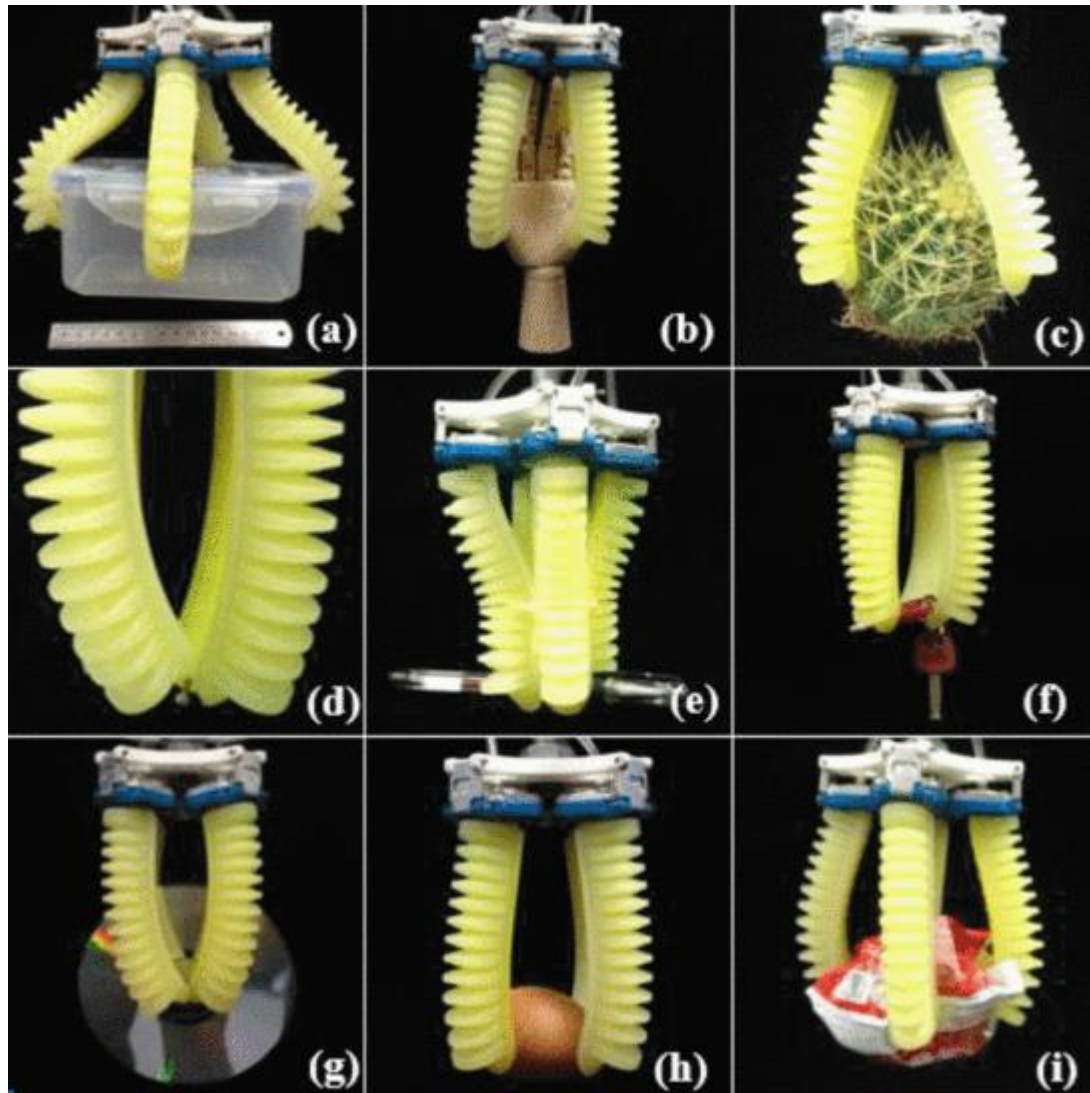


Figure 1-3: Shows the gripper's ability to pick up a variety of objects. (a) Tupperware (b) model of a human hand (c) cactus (d) screw (e) pen (f) keys (g) a compact disc (h) egg (i) bag of milk [11].

Although these examples represent a small population of existing soft grippers, they display the diverse handling potential of soft robotic grippers that can also be simple to control and cost effective, which makes them ideal for large scale production lines or human interactive devices [12]. The continued advancement of these soft grippers will allow for a vast range of geometrical shapes, weights, and materials that can be handled

by a single device, removing the need for re-tooling if ever there is a case. However, their operation can require high voltage [13-15] and/or long activation times that are not ideal for highly rapid and repetitive tasks such as those involved in manufacturing. In addition, these grippers are more ideal for macro applications and can be at a disadvantage when handling products on the micro scale.

1.3 MEMS Handling

Micro Electro Mechanical Systems (MEMS) are ubiquitous in the era of smartphones [16] and are delicate systems that require minimally invasive manipulation techniques when traveling through fabrication and/or assembly processes. These systems, called die, are often fabricated on thin silicone discs called wafers, and undergo fabrication processes such as photolithography and chemical etching. As devices become smaller wafers can become thinner. This makes them more susceptible to being bent or broken during handling due to the residual stresses in the layers formed during the manufacturing process which can in turn lead to lower yields. Carrier substrates can be introduced as a support mechanism for the wafer as it travels through the production process [17], but depending on fragility these may not always be effective. Commonly, MEMS devices are handled on the outside edges to prevent damage while being picked up and placed, and may require multiple tools, each being unique for specific operations and/or needs [18, 19]. A proven reliable method for handling MEMS devices is transfer printing, which is a process that focuses on the interfacial mechanics of the adherent ('sticky' object) and the adherand (substrate to be moved) and how to separate the two once the system has been positioned correctly [20, 21]. Transfer printing allows for a variety of MEMS to be

handled because it involves surface-to-surface contacts and natural adhesive properties, rather than the pinching or suction forces associated with micro-tweezers or vacuum wands. For example, Jefferey D. Eisenhaure et al. fabricated a stamp made of shape memory polymer (SMP)[22]. Glass transition temperature properties were used to manipulate micro structures on the bottom surface which resulted in a reversible dry adhesion device. By applying heat to the stamp and a compressive preload, pyramid shaped micro-points located on the bottom of the stamp are then able to retract into the stamp, increasing the contact surface area for a high adhesion state. The temperature is then lowered so the points remain concealed while the object is being transported to the final location. When positioned correctly, the stamp is heated without compression forces allowing the micro-tips to extend from concealment decreasing the contact surface area, resulting in a low adhesion state, and allowing the object to be placed down.

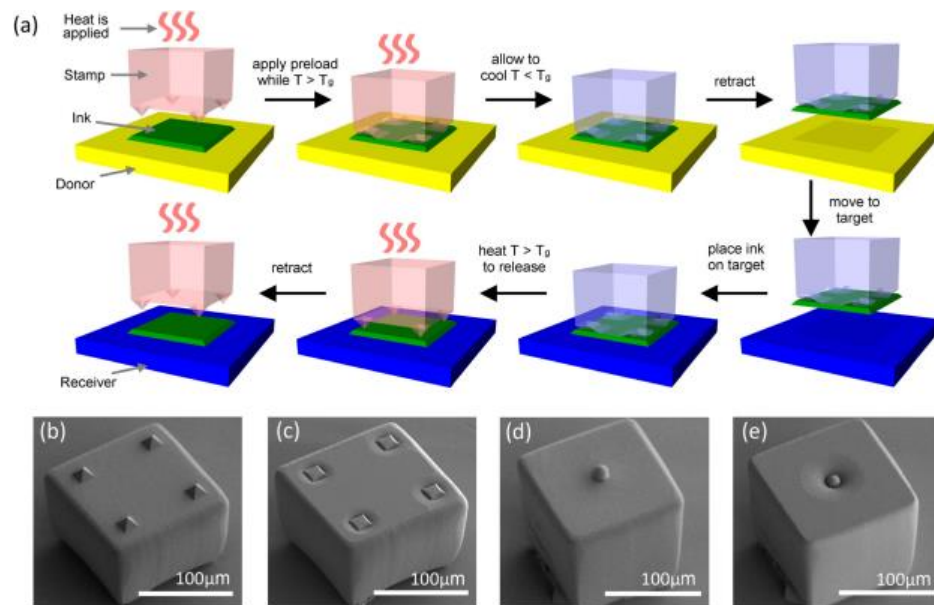


Figure 1-4: (a) The process flow for picking up and placing of an object with the stamp. (b) The stamp in a low adhesion state. (c) The same stamp in a high adhesion state. (d) Stamp with a dimple in the middle in a low adhesion state. (e) The dimple retracted results in a high adhesion state [22].

These SMP stamps can vary in size and geometry or be placed in an array so that multiple die can be picked up and selectively placed. Huang et al. and Eisenhaure et al. developed and fabricated devices with an array of SMP stamps in conjunction with a laser system that allows for localized heating and selective placement [23, 24]. Application of heat to the entire SMP array, and compressive preload, allows for multiple die to be picked up at once. Selective placing is then accomplished by the implementation of a laser for singular SMP heating which releases the die as shown in Figure 1-5.

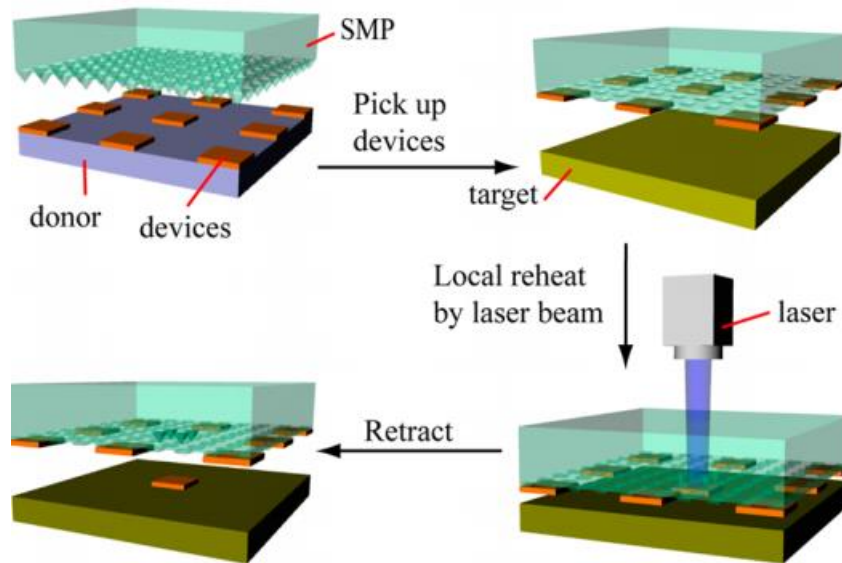


Figure 1-5: Schematic showing the multiple die pick up capabilities of the conical SMP stamp array and the use of a laser for localized heating, resulting in selective placement [23].

Other methods of transfer printing such as shear-enhanced [25], shown in Figure 1-6 and rolling stamp [26, 27], shown in Figure 1-7, have shown success and aid in providing custom processes that can be tailored to specific applications such as assembly. However, a device with universal handling characteristics that does not require outside influencers such as heaters or lasers, but rather is all inclusive, would be beneficial to the MEMS industry.

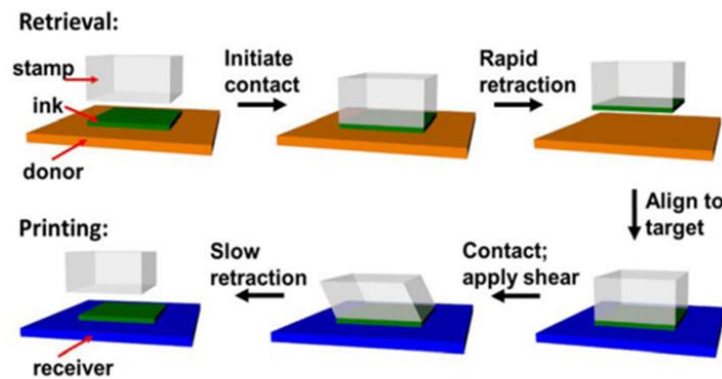


Figure 1-6: Process flow of shear transfer printing. An elastomeric stamp is brought into contact with the target which is then picked up and transported to the desired area. Once in position, the target is placed down and shear is slowly applied allowing the stamp to disengage resulting in placement of the target [25].

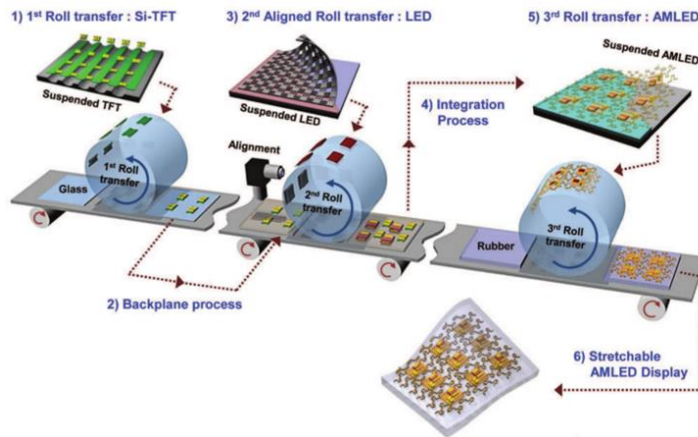


Figure 1-7: Schematic of a multi-roller transfer printing process [27].

1.4 Bio-inspired Adhesives

Nature is one of the primary sources of inspirations when it comes to designing devices that improve our capabilities. Simple things we take for granted, such as the human body, are so complex that it is difficult to mimic these naturally occurring systems. One fascinating phenomenon is the Gecko's ability to climb various surfaces whether smooth, rough, clean, or dirty. This variable adhesion mechanism has been the inspiration for many new adhesive films, and has the potential to be used in "the next-generation clean manufacturing technology" [28].

The Gecko's ability to climb surfaces stems from Van Der Waal's attractive forces between two atoms [29-31]. The foot of the Gecko contains an hierarchy of micro to nanoscale hair-like structures called spatula, shown in Figure 1-8, that are responsible for their climbing ability [32]. Each spatula (or setae) is capable of holding an average of 195 μN , meaning that a small portion of setae in contact is sufficient for proper adhesion [33].

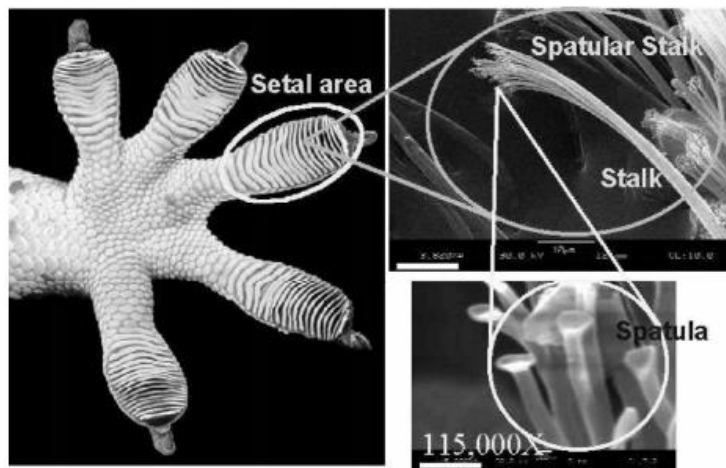


Figure 1-8: Left: shows the bottom of a gecko's foot. Right: the hierarchy of hairs called spatula that aid in the gecko's ability to climb multiple surfaces [32].

This hierarchal structure, if replicated, has many applications for macro soft robotic grippers and micro handling devices, and has been the driving inspiration behind biomimicry films [34, 35]. For example, Zhuxia Rong et al. successfully fabricated a biomimetic hierarchical structure consisting of polymer micro-posts topped with carbon nanotubes that are densely packed to resemble the bottom of a gecko's foot [36].

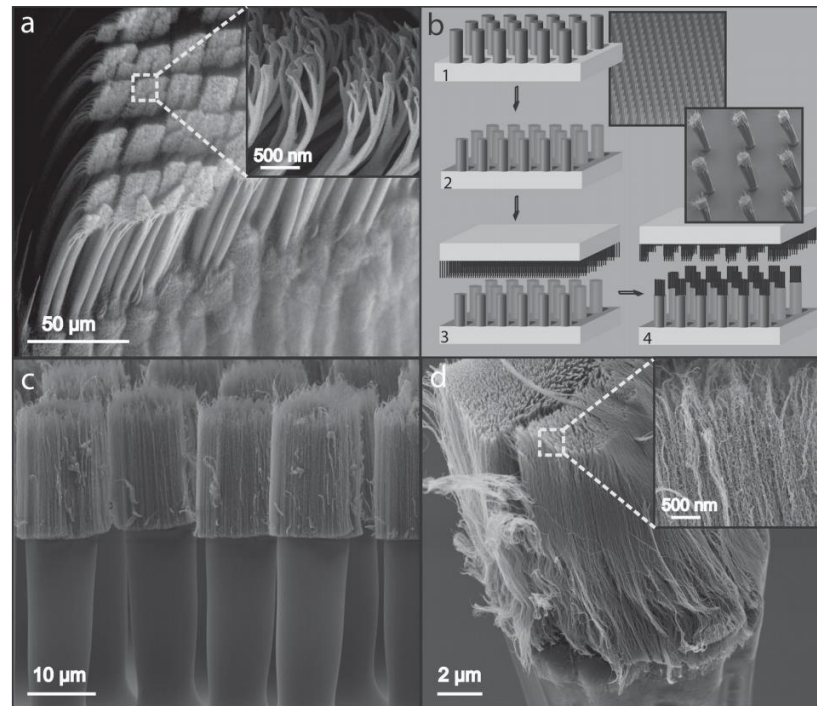


Figure 1-9: (a) SEM image of a gecko toe pad displaying the hierarchy of structure. (b) Fabrication process overview. (c) Polymer pillars with carbon nanotubes on the tips. (d) Magnification of the carbon nanotube tips [36].

Shear testing was performed on the hierarchical pillar arrays (HPAs) in comparison with a pure carbon nano-tube forest (CNTF). Results show that on rough surfaces, the HPAs perform nine times better than the CNTF due to the hierarchical structure which allows for better contact and conformity to a surface. The hierarchal benefits have also been

shown by Jongho Lee et al. who were successful in the fabrication of a device that consists of ‘flaps’ to mimic the lamellar arrays seen on a gecko toe, Figure 1-10. Each ‘flap’ has a nanofibrillar sub-array that provides adhesive properties. The result is a dry adhesive structure that is capable of holding 3 N of hanging weight while attached vertically to a stainless steel plate [37].

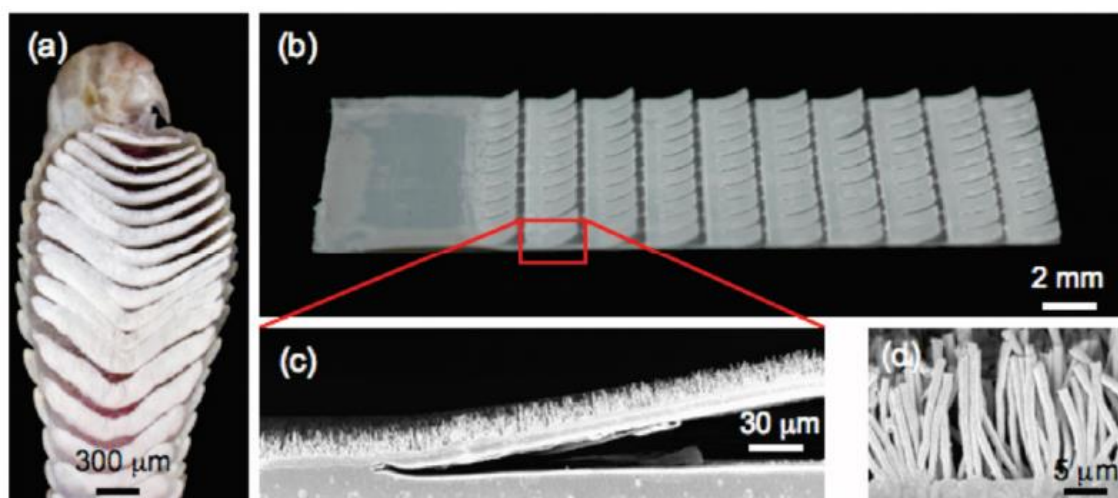


Figure 1-10: (a) Toe pad of a gecko displaying the lamellar arrays courtesy of Professor Kellar Autumn. (b) The fabricated device with similar lamellar arrays. (c, d) SEM imagery of the nanofiber arrays on lamellar flaps [37].

The gecko is not the only inspiration for biomimetic films. For example, the octopus-inspired adhesive pad developed by Lee et al. that is intended to be used for the handling of semiconductors or any other device that requires handling without the application of preload forces as seen with transfer printing. Muscle actuation of a suction cup is accomplished by the thermo-response of the hydrogel pad. When the temperature increases, it causes the hydrogel layer to shrink resulting in an increase in internal volume, thus effectively pulling a vacuum for suction to a target surface. Cooling the

hydrogel causes it to swell, thus decreasing the internal volume and removing the vacuum allowing for the surface to be released [38].

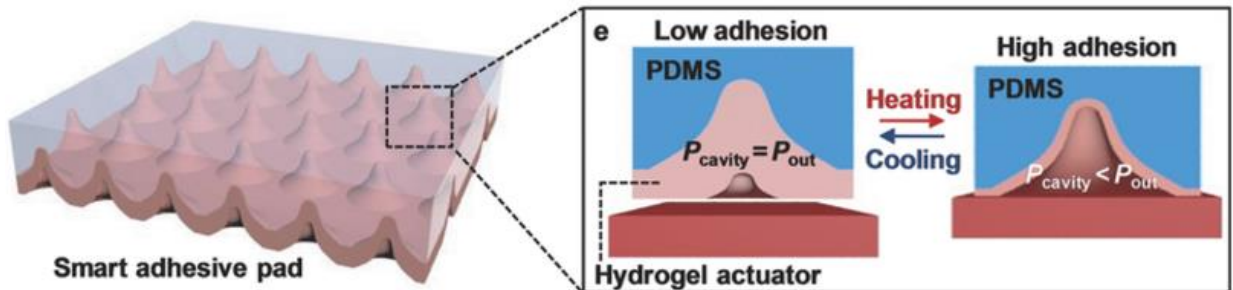


Figure 1-11: Octopus inspired film with “suckers”. When the hydrogel is heated, expansion of the inner chamber pulls a vacuum for suction to a surface. Then, cooling causes the hydrogel to swell decreasing the internal volume and releasing the vacuum and object. [38]

Bio-inspired adhesives display huge potential in applications such as handling devices whether micro or macro, but also increase and extend the capabilities of robots by unlocking wall climbing abilities [34, 39-41]. For example, three types of climbing robots: gecko-like, tank-like, and wheel-leg robots have shown great success in their abilities to scale vertical surfaces using the bio-inspired films [42].

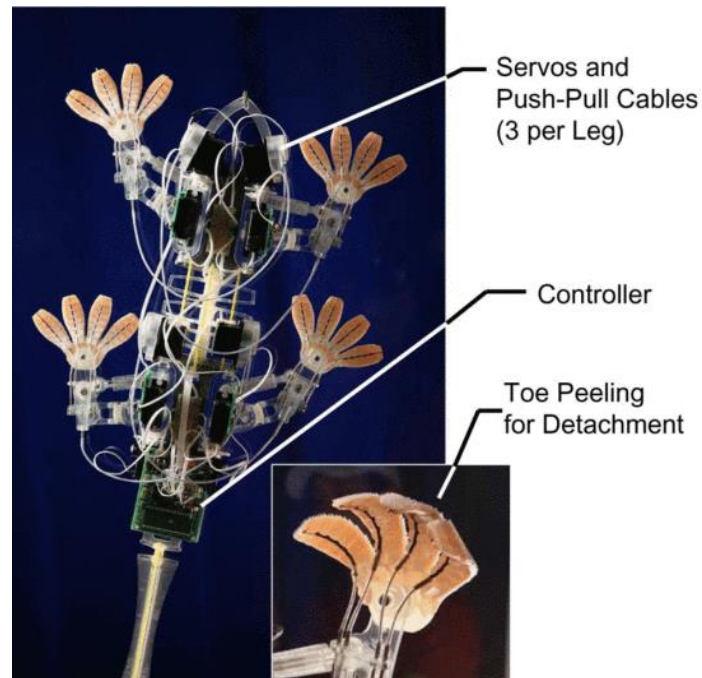


Figure 1-12: A gecko-inspired wall climbing robot with fibrillar adhesive pads on the feet. Actuators on the toes allow for an upwards toe peeling motion similar to a gecko [43].

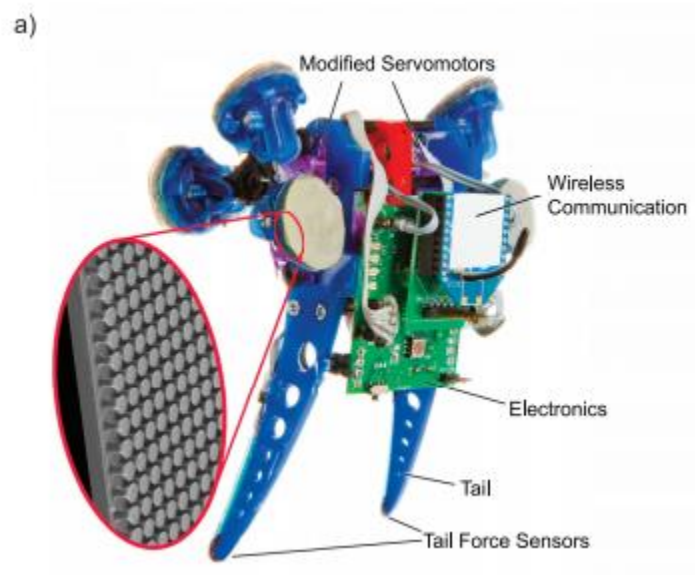


Figure 1-13: Wheel-like robot with mushroom tip fibrillar arrays on the pads [44].

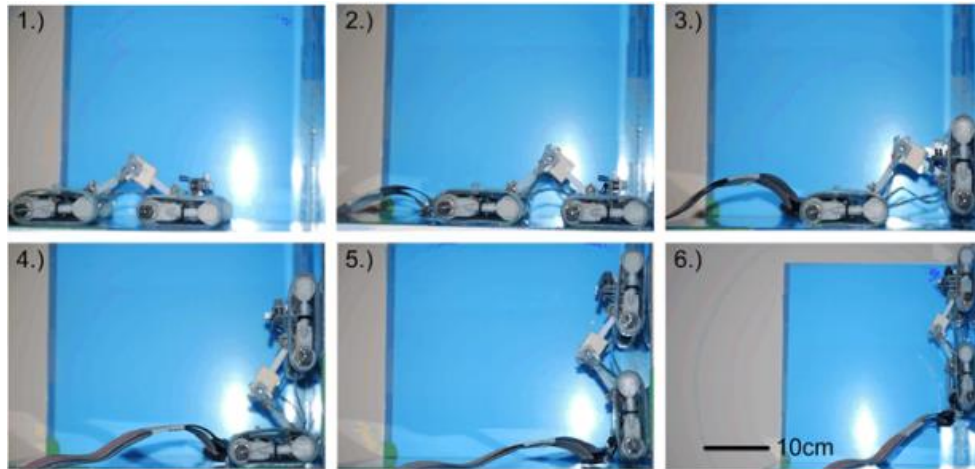


Figure 1-14: Tank-like wall climbing robot with bio-inspired adhesive treads scaling a vertical surface [45].

These bio-inspired adhesives no longer apply to just small robots as shown by Hawkes et al. who successfully developed and fabricated gecko-inspired adhesive pads that allow for a human to climb a vertical wall. This device is successful in showing that the hierarchal adhesion concepts of the gecko's ability to climb surfaces can be scaled for human use [46].



Figure 1-15: Three frames of a video showing a 70kg climber scaling a vertical wall with the gecko-inspired adhesion system [46].

There is an ever increasing need for handling or manipulation devices. Soft robotic grippers currently allow for objects varying in shape, size, and weight to be manipulated by one gripper rather than having multiple handlers, but can often require high voltage or long activation times. As MEMS devices continue to become smaller and more fragile, reliable delicate handling processes are required for precision assembly and to ensure high yield of devices. Current manipulation techniques, some employing tunable adhesion, are sufficient but can require the use of compressive forces for handling which may result in breakage depending on the delicacy of the component. External instrumentation may also be required which could lead to sophisticated systems versus a more all-in-one package that could be more beneficial. Biomimetic adhesive devices and films provide more options, such as smooth or rough surfaces, in the field of both macro and micro handling, but lack in the ability of a wide range of tunable adhesion disallowing users to customize the desired adhesion force per experiment. Our research into completely reversible tunable dry adhesion will provide a novel device that has fast actuation, scalability, an inclusive stand-alone package, and adhesion customization that will expand the capabilities of handling devices with tunable dry adhesion.

Chapter 2 – Background

2.1 Introduction

This section will introduce the concept of reversible tunable dry adhesion and provide a few examples of capable devices. Reversible tunable dry adhesion can be accomplished through the manipulation of material properties but done so in such a way that the original properties remain un-affected by the process. This ensures the device can be used multiple times. Material properties such as critical fracture toughness and critical energy release rate and the role they play in regards to crack propagation will be introduced followed by an overview of the main goal of the project.

2.2 Tunable Adhesion

Tunable adhesion is the ability to manipulate the ‘stickiness’ of a component, typically of elastomer, to be lower than that of its natural state. To achieve reversibility, this change in adhesion should be done in such a manner that the natural state of the adhesive is not affected by the manipulation process. This is important if the device needs to be used repeatedly, which is where dry adhesion is beneficial. Dry adhesion pertains to not using any additives, such as glue and epoxies, to increase adhesion, or release agents to lower it. To obtain reversible tunable dry adhesion, material properties, interfacial mechanics, phase changes, and temperature are controllable factors that can influence the system.

Material properties, such as magnetic properties, can be exploited to tune adhesion [47, 48]. Northern et al. developed a film that utilized the magnetic properties of nickel. The film contained nickel cantilevers that were coated with polymer nanorods which provided adhesion. When the film was in an “ON” state with no magnetic field, the nanorods are

exposed making the film ‘sticky’. To then turn “OFF” the adhesion, a magnetic field is applied causing the nickel beams to rotate in such a manner that the polymer nanorods are covered, effectively reducing adhesion [49].

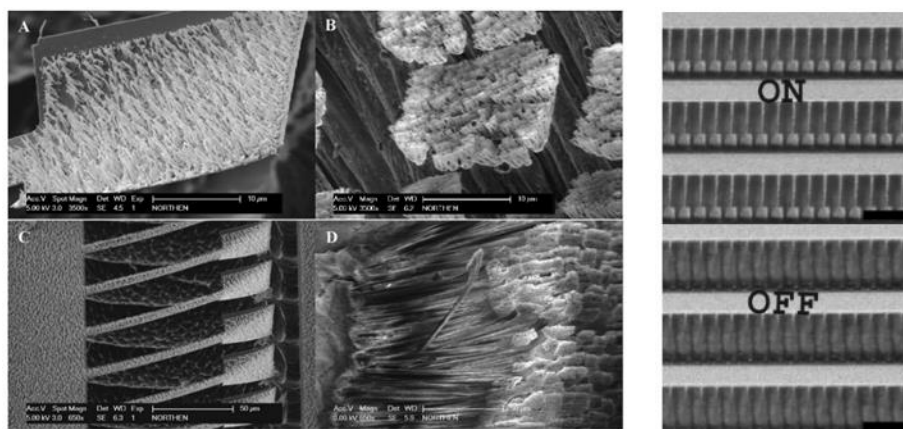


Figure 2-1: (a) Nickel cantilever with polymer nano-rods on the surface. (b) Magnification of a gecko foot setae branch with spatulae at the end. (c) Polymer nano-rod coated nickel cantilever array displaying hierarchical mimicry when compared to (d) a setae array of a gecko foot. Right: Top shows the cantilevers under no magnetic field exposing the polymer nano-rods in an adhesion “ON” state. Bottom shows the introduction of a magnetic field resulting in the cantilevers rotating and covering the nano-rods in an adhesive “OFF” state [49].

Zhou Ye et al. were successful in obtaining reversible adhesion by placing a droplet of liquid Gallium at the tip of an elastomer post, and using the phase change properties of Gallium to reverse adhesion. This was done by applying heat to the system which allowed the Gallium to conform to an opposing surface to be picked up. Once the surface was determined to be in sufficient contact with the Gallium droplet the temperature was lowered such that the Gallium could solidify causing a strong bond on the interface [50]. To release from the interface, heat was again applied to the system causing a phase change in the Gallium allowing the post to be removed.

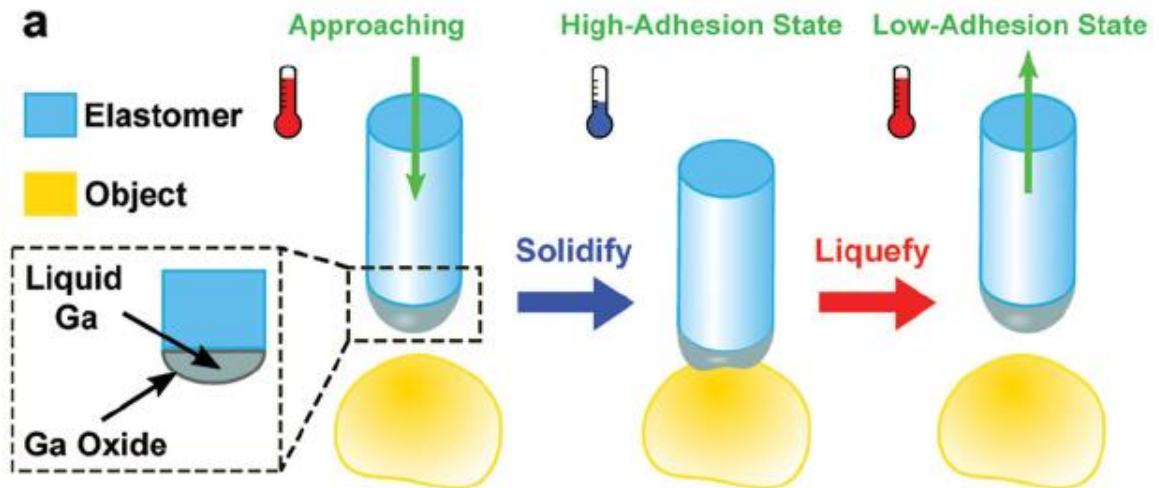


Figure 2-2: Schematic showing the test setup for the reversible switchable adhesion device. Heat is applied allowing the liquid Gallium to conform to the desired surface. The system is then cooled to solidify the Gallium resulting in temporary adhesion. When adhesion is no longer required heat is then applied liquefying the Gallium and releasing the bond between the elastomer post and the surface [50].

Yue Wang et al. investigated switchable dry adhesion by experimenting with step-like elastomer posts that focus more on the peeling motion of the device [51]. The posts were placed face-up and a surface was brought down onto the posts, Figure 2-3. After a preload was applied the drag direction could be selected. The pillars were dragged either left or right before pulling the surface away. Depending on the drag direction, contact surface area was either reduced or increased (Figure 2-4), resulting in a reduction or increase in pull-off force respectively.

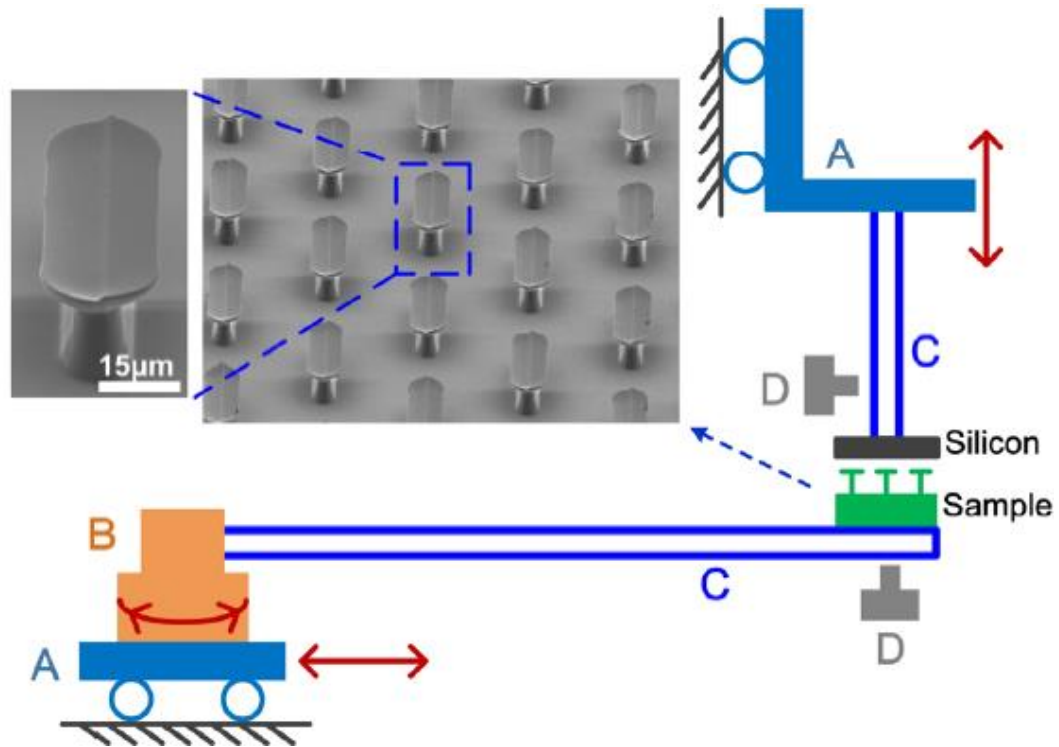


Figure 2-3: Shows the test set up for the step-like micro pillars. The system can move in the x direction allowing for the user to define the direction of drag to obtain the desired increase or decrease in adhesion [51].

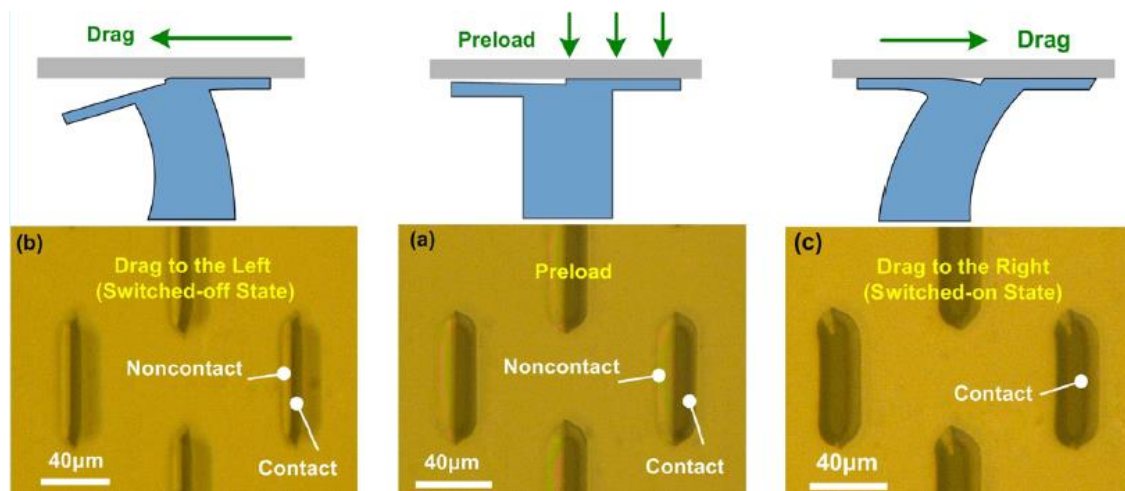


Figure 2-4: Shows how the step-like post reacts to the drag direction. By dragging to the left a reduction in contact surface area occurs resulting in reduced adhesion. By dragging to the right an increase in contact surface area occurs resulting in increased adhesion [51].

Similarly, Seo et al. developed a reversible dry adhesive film that utilized micro SMP wedges. The process, shown in Figure 2-5, starts with placing the target object on the film. Next, heat is applied to the micro SMP wedge array, and when the glass transition temperature of the SMP has been reached, a preload is applied. This causes the wedges to deform, thus increasing the contact surface area. Preload is maintained while the array is cooled below the glass transition temperature so the wedges keep the deformed shape. Once cooled the target object is ready to be manipulated. To remove, the array is heated again, and the preload is released allowing the wedges to return to the original geometry. [52].

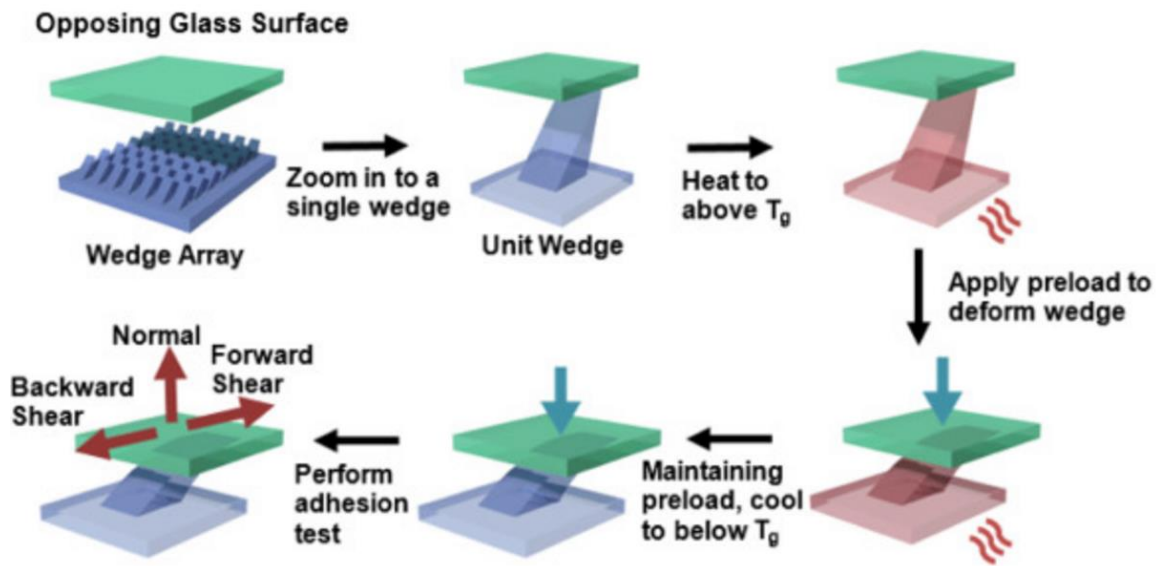


Figure 2-5: Schematic of the adhesion process starting with a cooled micro SMP array. Heat is then applied along with a preload to deform the wedges resulting in a high adhesion state. To maintain this state, the array is cooled causing the wedges to remain deformed for high adhesion allowing the target object to be manipulated [52].

Another way that adhesion can be tuned by manipulating contact surface area was shown by Jeong et al. through surface wrinkling in combination with micro-pillars. In the film's resting state it is wrinkled, which causes the PDMS posts to tilt resulting in a point contact and an adhesion "off" state. To achieve an adhesion "on" state, the film is stretched to make the posts align perpendicularly, allowing for a surface contact resulting in a high adhesion state.

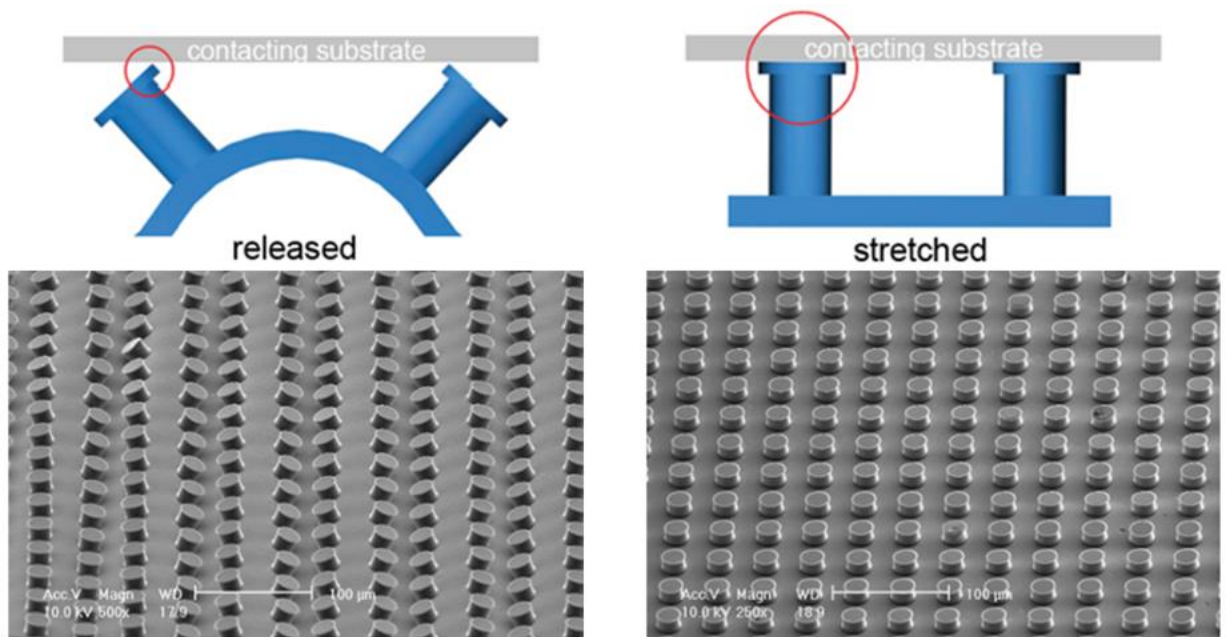


Figure 2-6: Left: The film in an adhesion off state due to the posts making a point contact because of surface wrinkling. Right: The film in an adhesion on state. Stretching the film allows the posts to make a surface contact increasing adhesion [53].

Recent work by H. K. Minsky and K. T. Turner at the University of Pennsylvania shows that by introducing a rigid core into an elastomer post and controlling the shear direction, tunable dry adhesion can be accomplished. This is a result of shifting the peak stress from

the edge of the sample to the center, aiding in the achievement of optimal adhesion of the elastomer post to the surface [54].

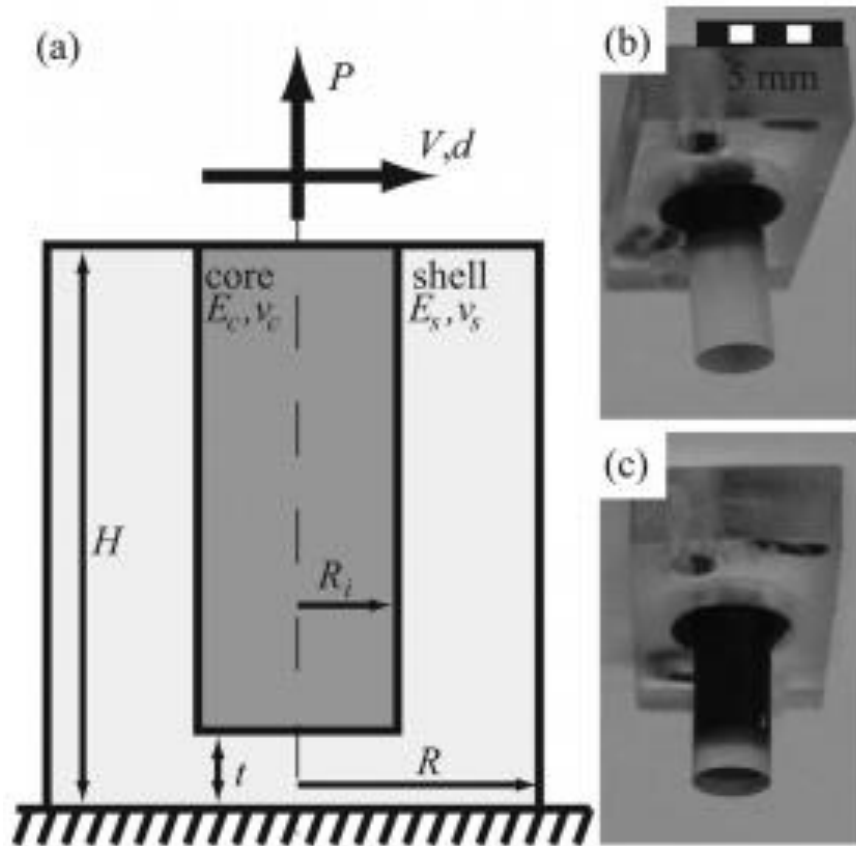


Figure 2-7: (a) Elastomer post with rigid core diagram (b) PDMS post without a rigid core (c) PDMS post with a PEEK core [54].

The findings of this work inspired collaboration between Dr. Kevin Turner and Dr. Wanliang Shan who explored the idea of employing a tunable rigid core to achieve dynamically tunable dry adhesion in a soft core-shell composite structure. This was done by embedding a cPBE within a PDMS post shown in Figure 2-8. Preliminary testing of the tool also indicated promise of a multi-level dynamic tuning device (Figure 2-9) [55].

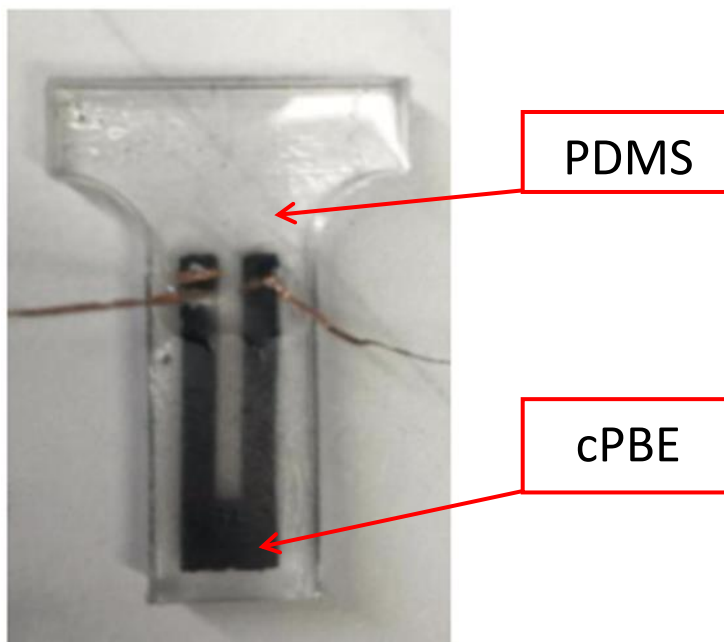


Figure 2-8: An elastomer post with a tunable cPBE core. Normally the core is rigid and upon activation by applying a voltage, the core becomes soft allowing the sample to stretch.

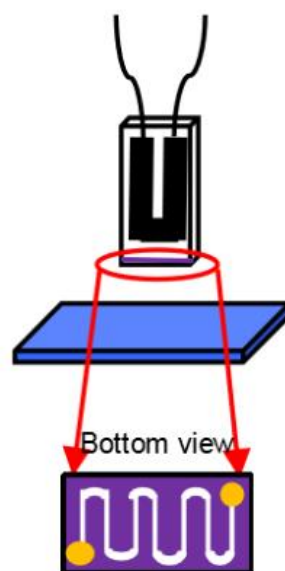


Figure 2-9: The schematic of the combined tunable core (Black) and variable stiffness interfacial heater (Purple) injected with LMPA (White). This device allows for multi-level dynamic tuning of dry adhesion. [55].

The final device will be semi-all-inclusive with just the need of a power supply for the multi-level activation. The ability to tune both the core and the interface will allow for crack propagation mitigation leading to customized settings for varying applications. The device will be quick to activate and require lower voltages making it an ideal candidate as an attachment for soft robotic grippers. With the correct fabrication processes and further research, the device can be scaled for either micro and macro applications such as MEMS handling or wall climbing technology.

2.3 Theory

Because dry adhesion involves the bonding and de-bonding between two surfaces, fracture mechanics plays a major role in describing the mechanisms of this interfacial interaction. The separation of two faces, or fracture (crack growth), can be described by three modes: Mode I, Mode II, and Mode III, shown in Figure 2-10. When a material experiences pure Mode I loading, the critical energy release rate, G_C , needed for crack propagation is lower than that of the same material experiencing Mode II, III, or any mixed-mode loading shown in Figure 2-11 [56].

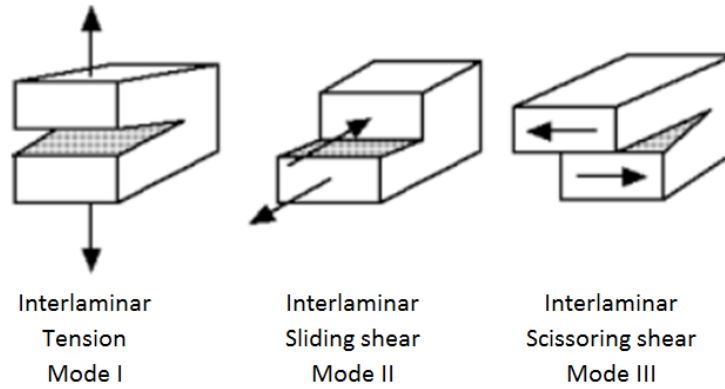


Figure 2-10: The three Fracture Modes associated with crack growth Tension, Sliding Shear, and Scissoring Shear [56].

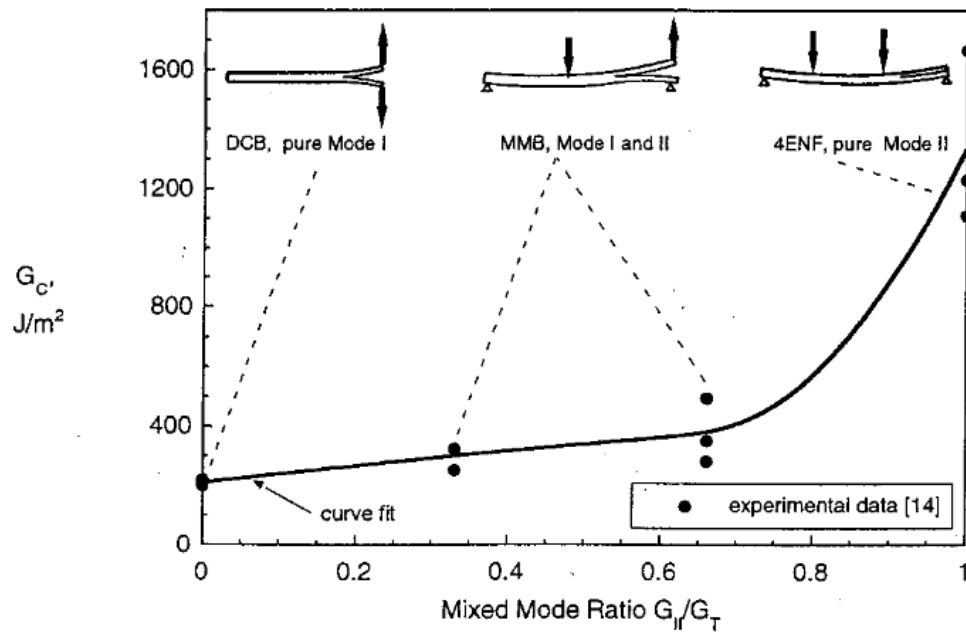


Figure 2-11: Experimental data for a specific material and the increase in G_C that is required for crack growth as the sample experiences different modes [56].

Materials have a natural resistance to fracture called “fracture toughness”, K_C , such that when the applied load causes the stress intensity factor, K , to become larger than that of K_C the crack will grow. Assuming that pure Mode I was experienced during testing and

as the critical fracture toughness is the lowest for Mode I in comparison to Mode II, III, or any mixed-mode loading, K_I was usually considered to be compared with K_C when determining crack growth. Alternatively, the fracture criteria G , the “energy release rate”, can be considered, where G is given by

$$G_I = \frac{K_I^2}{E'}, \quad (1)$$

where $E' = E/(1 - \nu^2)$ with E being the Young’s modulus, ν the Poisson’s ratio, and K_I depends on the geometry and location of the crack. With the energy approach, fracture criterion can be given as

$$G \geq G_C,$$

with G being the available energy release rate of the crack and G_C is the critical energy release rate required to propagate a crack [57].

For example, a 2D pure PDMS post was modeled in ANSYS and subjected to a tension load of 28 kPa. The resultant maximum strain at the crack tip was calculated to be 1.0203 correlating to a G value of $3.63 \frac{J}{m^2}$. The G_C value reported at low pull-off speeds and room temperature for pure PDMS in Ref. [21] is roughly $3.6 \frac{J}{m^2}$ (Figure 2-12). It means that under this loading, $G \geq G_C$ and thus the crack will propagate.

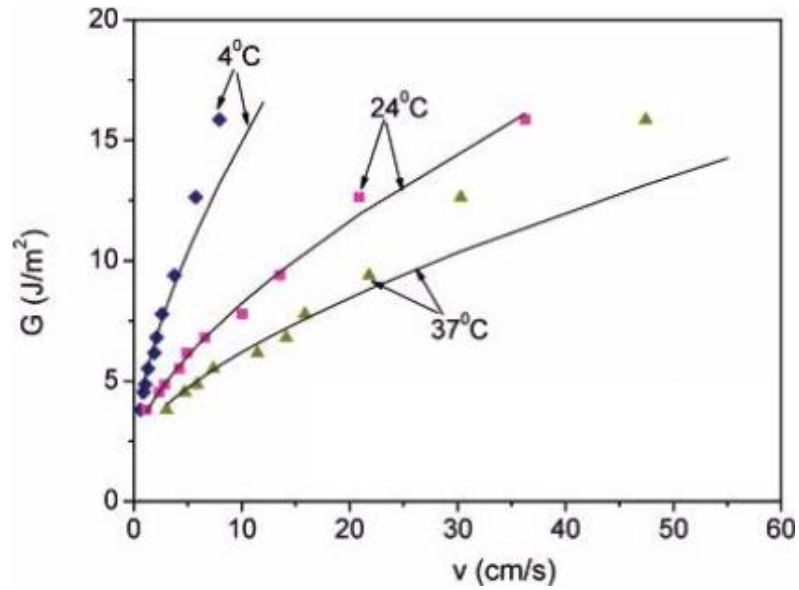


Figure 2-12: The critical energy release rate for pure PDMS at different temperatures. [21]

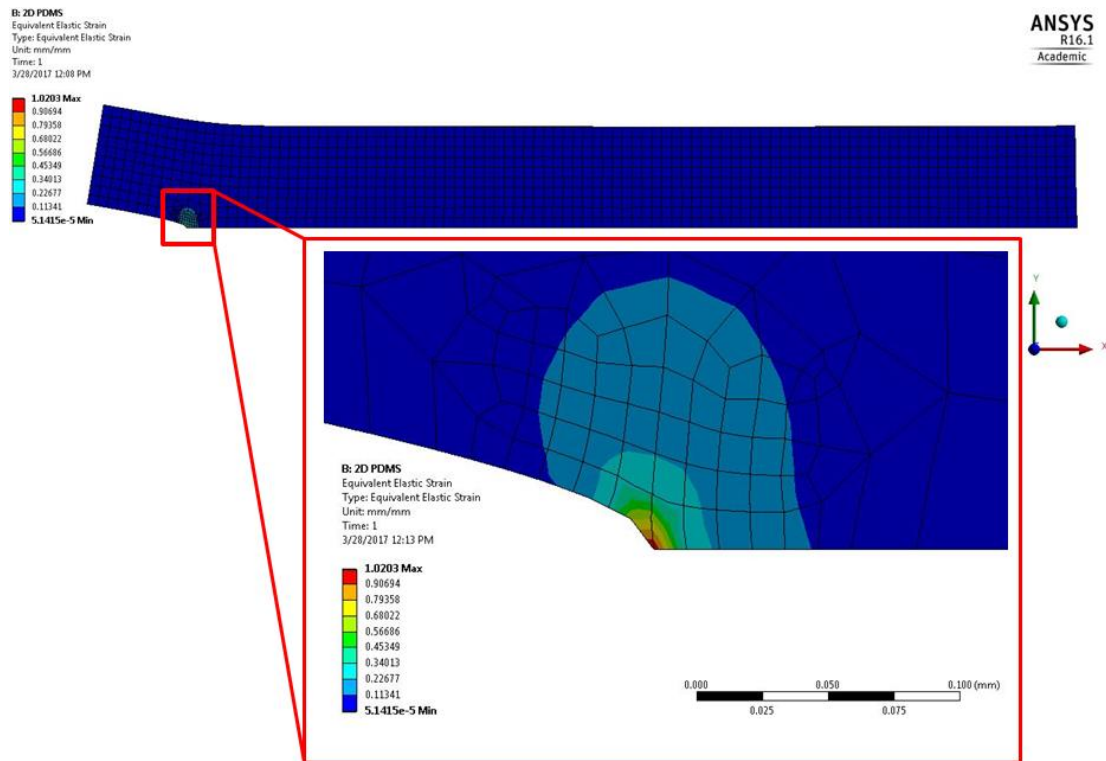


Figure 2-13: Simulation of a 2D pure PDMS post under a 28 kPa tension load. Results show a maximum strain at the crack tip of 1.0203, resulting in a G equal to G_c meaning that the crack will propagate.

If a PDMS post with the exact same geometry as described in the previous paragraph contains a rigid core embedded 200 μm deep from the bottom surface and with the same load applied, the result is a maximum strain at the crack tip of 0.2318 giving a calculated G of $0.1644 \frac{J}{m^2}$ resulting in $G < G_C$ meaning that for the crack to propagate, a higher load should be applied.

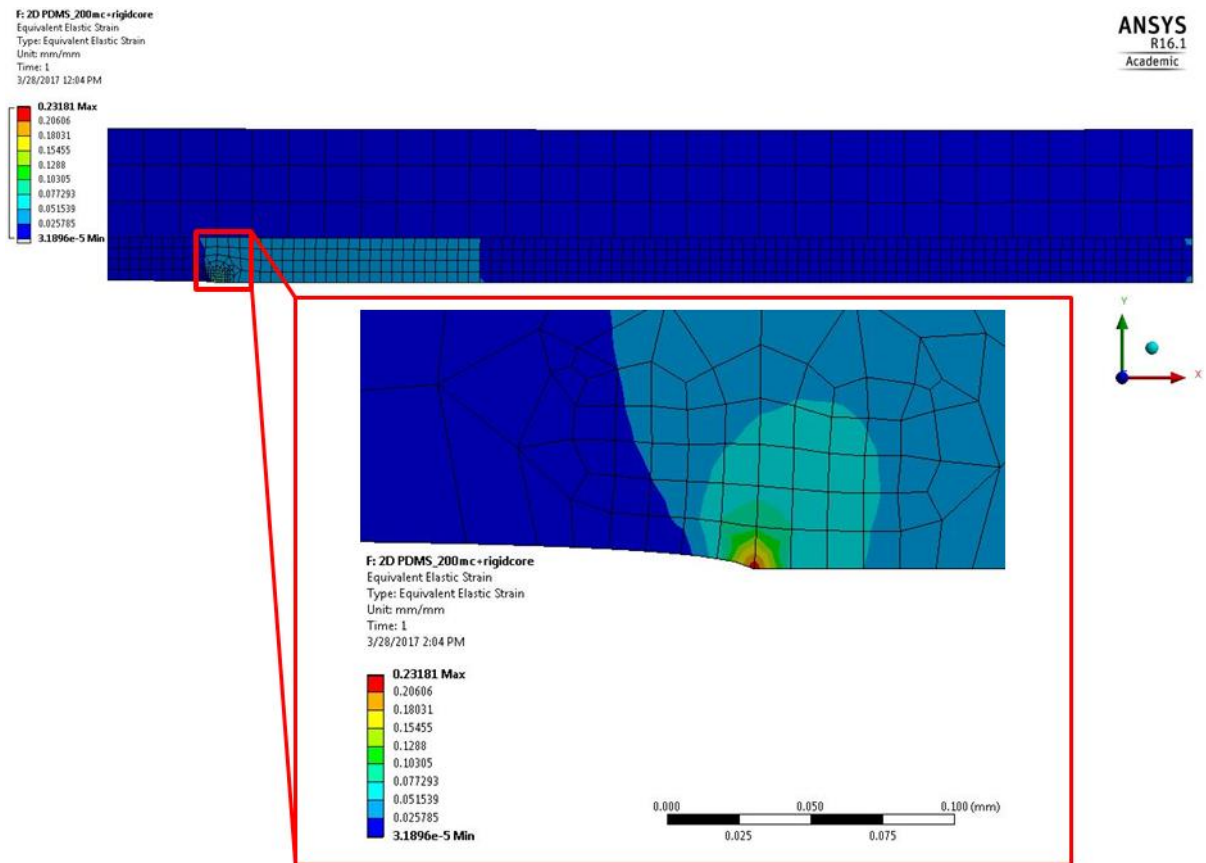


Figure 2-14: PDMS post with embedded rigid core subjected to the same 28 kPa tension load. Results show a more uniform strain distribution resulting in a lower maximum strain value of 0.2318 giving a G lower than G_C meaning that a higher load would need to be applied to propagate the crack.

Furthermore, a higher maximum stress can be seen in the pure PDMS post, while the rigid core embedded post experiences a more uniform stress concentration resulting in a lower maximum stress experienced. Inherently a higher deformation is observed in the pure PDMS sample than that with the rigid core. This is important because lower deformation reduces the strain, thus reducing G and requiring higher applied loads for crack propagation in samples with rigid cores. Effectively, this means the dry adhesion is increased.

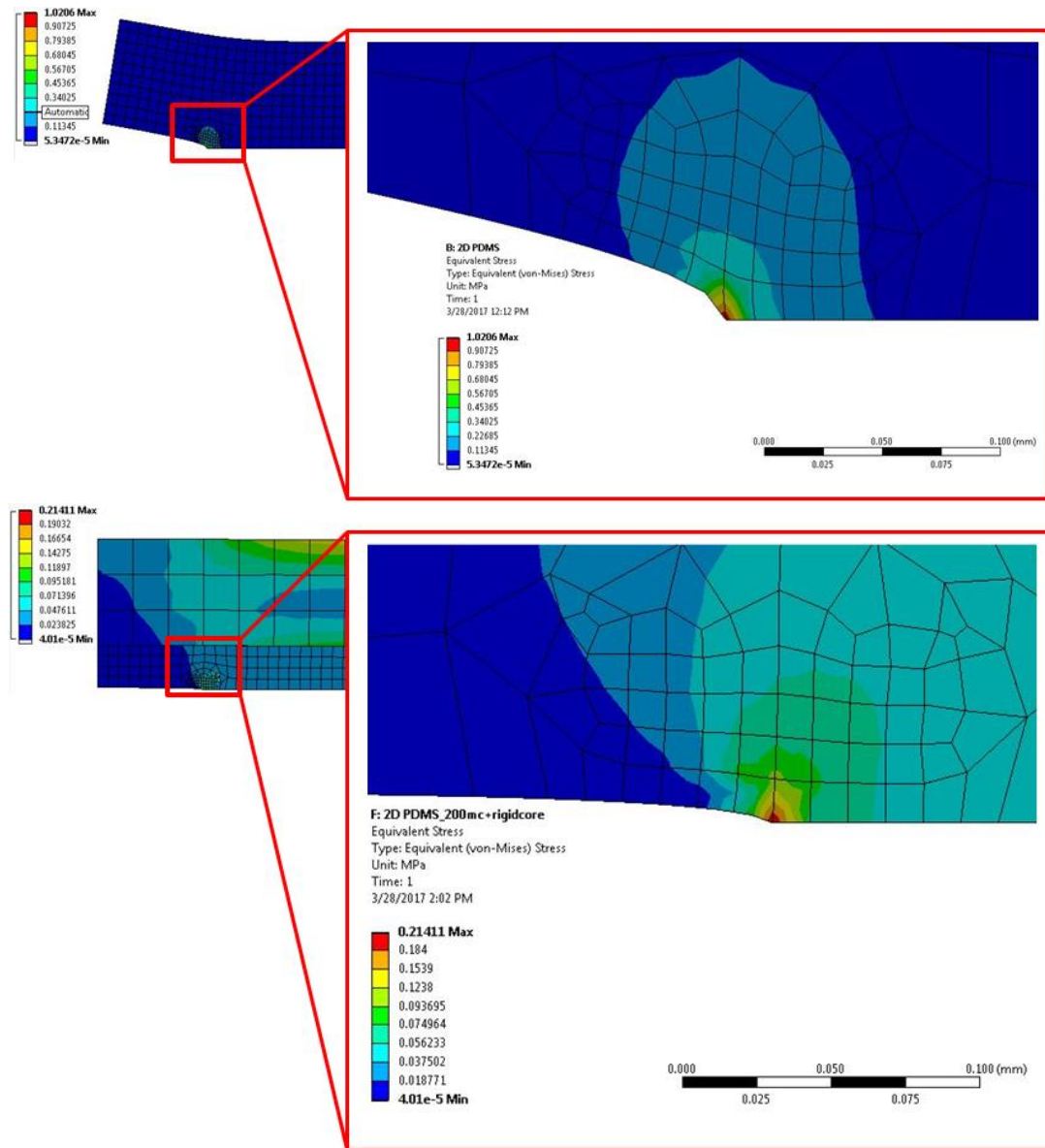


Figure 2-15: Top: stress distribution of the pure PDMS post with a max stress of 1.0206 MPa. Bottom: More uniform stress distribution of the PDMS post with embedded rigid core with a max stress of 0.2141 MPa.

B: 2D PDMS

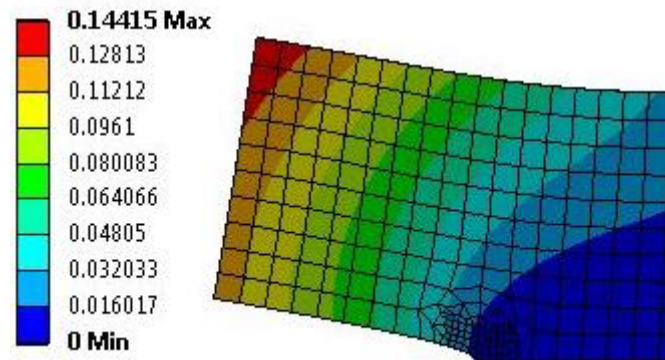
Total Deformation

Type: Total Deformation

Unit: mm

Time: 1

3/28/2017 12:10 PM

**F: 2D PDMS_200mc+rigidcore**

Total Deformation

Type: Total Deformation

Unit: mm

Time: 1

3/28/2017 12:05 PM

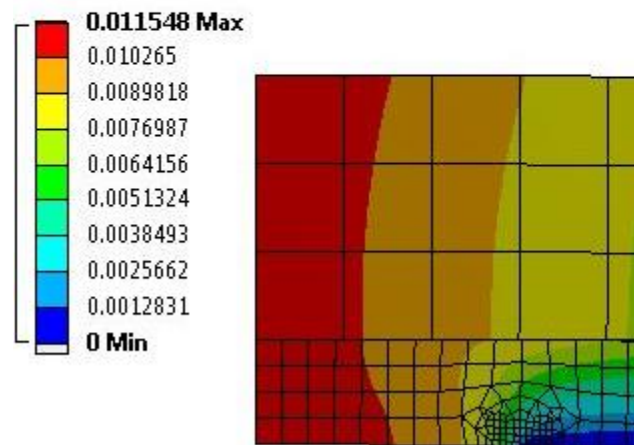


Figure 2-16: Top: Deformation of the pure PDMS post with a maximum displacement of 0.14415 mm. Bottom: Deformation of the PDMS post with rigid core having a maximum deformation of 0.011548 mm. By reducing the maximum displacement experienced by a sample, strain can be minimized thus keeping G lower for higher applied loads resulting in a change of dry adhesion.

2.4 Project

The focus of this thesis is to design, fabricate, and test a successful device to investigate the effects of variable rigidity on dry adhesion forces. A soft gripper fabricated with micro-channels injected with LMPA contained in a solid PDMS post is the prototype for testing. Using an Instron testing machine the effects of rigidity change on strain energy are studied.

With the LMPA solid at room temperature acting as a rigid plane, deformation at the interface should be more uniform and the maximum stress and strain at the crack tip will be lower, yielding a higher value for pull-off force when un-activated. When the device is activated with an electrical voltage, the LMPA should reach a temperature to melt, allowing the sample to deform more with less uniform stress and strain distributions at the crack tip, which results in a lower pull-off force. This ability to manipulate the rigid plane in real-time should result in a completely tunable reversible dry adhesion device.

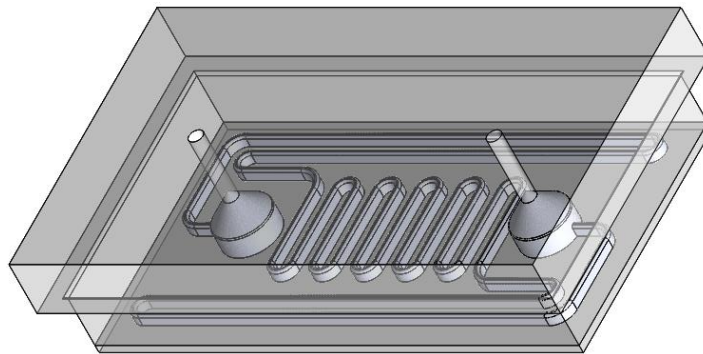


Figure 2-17: PDMS main body with LMPA filled micro-channels.

Chapter 3 – Design and Fabrication

3.1 Introduction

Throughout the experiment, fabrication proved to be the most challenging aspect. Layers would delaminate allowing liquid metal or LMPA to leak out of or across the channels rendering the device useless. Occasionally when curing, components would move out of plane with respect to each other giving an un-usable, misaligned device unfit for testing. Devices would lose resistance with no visible indication as to why. When the project began, the goal was to make a soft heater using liquid metal but quickly took a different path with the application of rigidity tuning. Micro-channel patterns, geometries, and fabrication methods were all experimented with before finally developing a repeatable, reliable enough process to create testable devices.

3.2 Design

Originally, the goal was to investigate the effects of an applied interfacial temperature gradient on dry adhesion. It was speculated that by raising the temperature at the interface, pull-off forces could decrease. A plan was devised to fabricate a soft heater with micro-channels injected with Gallium-Indium eutectic (EGaIn), a liquid metal, which could then be attached at the bottom interface of a pure PDMS post. Testing would then include the sample being brought into contact with a glass surface and a compressive pre-load applied. Then with the device activated by voltage and the liquid metal filled micro-channels acting as a resistor, heat would be generated to decrease the pull-off force. However, many failed attempts at producing a reliable soft heater that could perform under the repeated loading and unloading proved challenging.

When a device with adequately filled micro-channel was fabricated, activation of the device typically resulted in the formation of voids in the channels which ruined it. This event was also witnessed by Je et. al. who designed two heaters and found that the void formation is caused by differing thermal expansion coefficients between the PDMS and the EGaIn [58] . The first heater was of similar design, being a non-pressurized sample, meaning that the channels were injected with liquid metal and sealed. The second heater was pressurized providing a constant flow of liquid metal during operation. If activation did not ruin the device, usually the combination of activation and subjugation to a compressive load would often lead to a rupture and leakage of liquid metal.

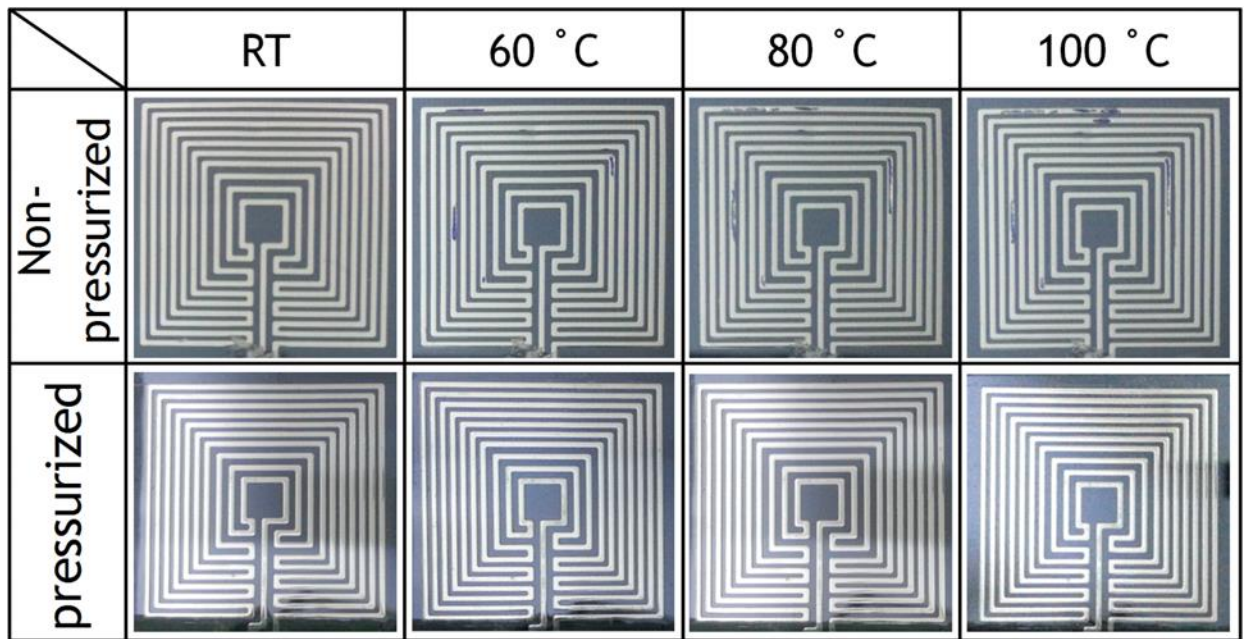


Figure 3-1: Top: shows a similarly sealed liquid metal heater and the formation voids at high temperatures due to different thermal expansion coefficients of the PDMS and EGaIn. Bottom: shows a liquid metal heater that is exposed to a constant a flow of liquid metal, filling the voids as they form [58].

The inherent drawbacks of the liquid metal soft heater design (for this application) led to the decision to re-design the device to a similar concept and use low melting point alloy instead of liquid metal. This would allow the device to switch between rigid and soft states, allowing the fracture mechanics at the surface and effects of a tunable plane to be studied.

The first version of the device, Figure 3-2, was a clone of that developed by Schubert et. al. seen in Figure 3-3 [59]. Although fabrication was successful and the sample was durable enough for testing, the channel pattern and dimensions were not conducive for the fracture mechanisms being studied to noticeably influence the system. Because of this, the LMPA channel pattern was re-designed to place the channels closer to the edge of the sample to increase the device's effectiveness in combating crack formation.

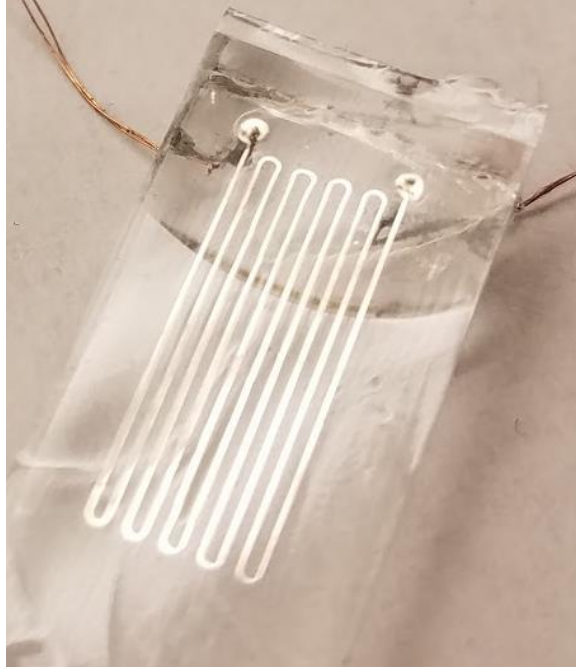


Figure 3-2: First version of the variable stiffness device. Channels were not close enough to the edges to allow the tunable plane to influence the system.

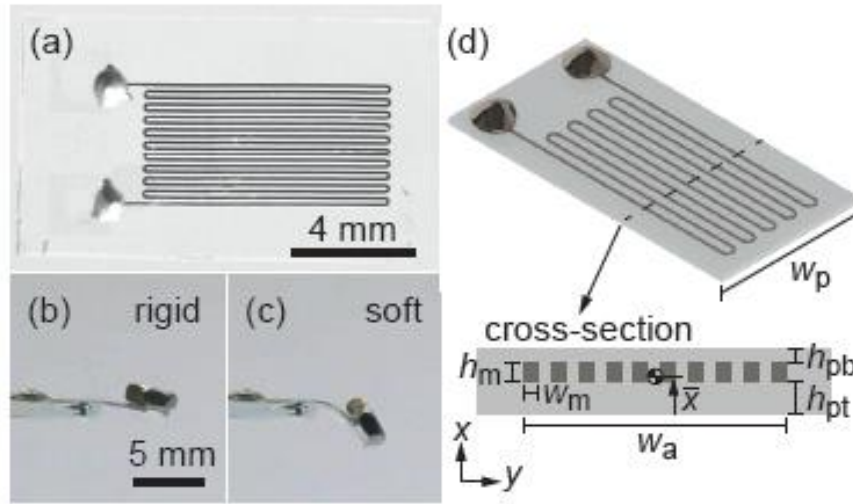


Figure 3-3: (a) Layout of the variable stiffness device. (b) Non-activated LMPA channels displaying rigid characteristics. (c) When activated, the LMPA goes through a phase change from solid to liquid allowing the device to bend. (d) Cross section of the device [59].

The crucial areas were the spaces between the edge of the sample and the channels, along with the space between the channels themselves. Complete delamination in these low contact surface area locations was prominent along with inter-channel breaches and/or leaks occurring during the injection of LMPA. Channel height was also an issue being that the shorter the channel, the higher the chance of resistance loss because of the lower amount of material allowed in the channel.

The edge spaces and channel heights started as low as 100 μm and were gradually increased until a sample robust enough to test was created. The final design had 200 μm wide LMPA channels that were 400 μm tall and 700 μm from any outer edge with an internal spacing between channels of roughly 500 μm . The short edge of the device was 9.12 mm and the long edge 17.17 mm. Channel height was 400 μm tall with a total length of about 122 mm.

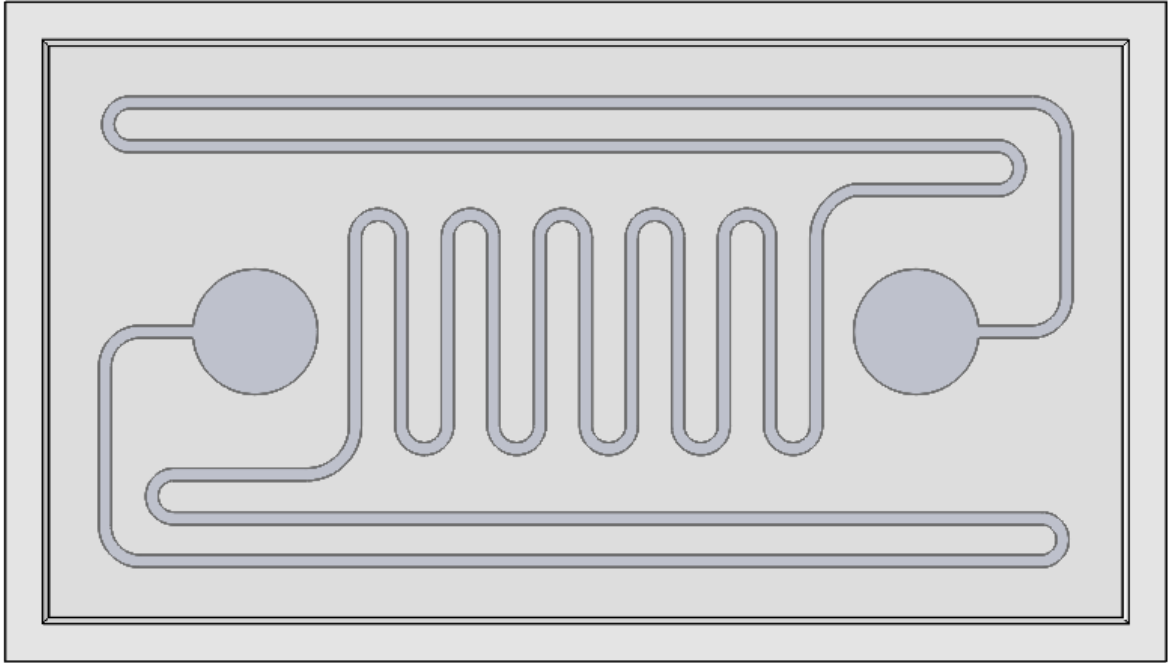


Figure 3-4: Bottom view of the final device design. LMPA channels were designed to be as close to each other and the edge as possible while maintaining device integrity for testing.

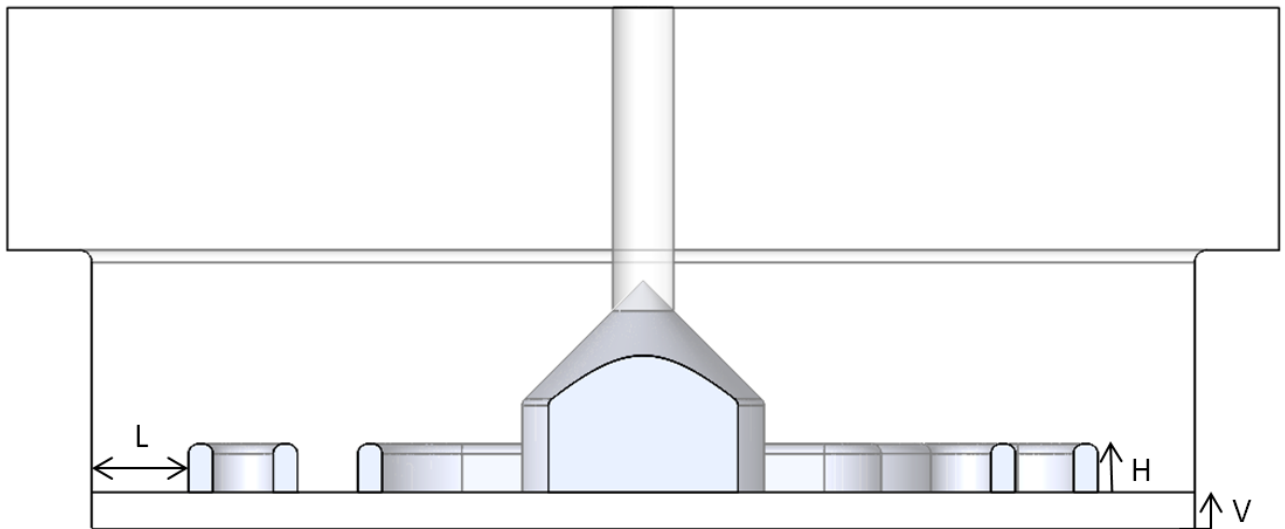


Figure 3-5: Cross sectional view of the main body with 200 μm wide channels where $L = 700 \mu\text{m}$, $H = 400 \mu\text{m}$, and V was varied from 200 to 1200 μm . Electrode wells have a conical shape to help keep material in the channel under compressive loading.

3.3 Fabrication Methods

The beginning stages of fabrication involved those outlined by Seigel et al. [60]. A copper substrate was cleaned and polished to decrease surface contaminants and roughness to allow for bonding of the photoresist. Single or combined layers of Riston Dry film photoresist (FX920 and FX940) were attached to the substrate with a laminator (Tamerica Tashin TCC-600). A mask was aligned and placed on top of the photoresist for UV exposure and curing. Once the channels were cured and developed, they were placed in a casting mold where PDMS was poured over the top, de-gassed in a vacuum chamber, and cured in an oven at 85°C for 1 hour.

Using this method did result in some successful units. However, the molds had a limited lifetime before the photoresist would begin to peel off requiring the fabrication of new molds. In addition, during the infant stages of the design, geometry alterations occurred quite frequently which would require new masks to be printed subsequently losing time. Channel height was also limited because only two layers of photoresist could be stacked on each other before the process became too difficult. Even the stacking of two layers often led to poor lamination or issues of over/under curing and developing. It soon became prevalent that better control of channel height, quicker production time for geometry changes, and a highly re-usable mold was needed to keep pace with the dynamics of the project. The need for rapid manufacturing became apparent and it was decided to utilize additive manufacturing by implementing the 3-D printer (Stratasys Objet24). This allowed for experimentation with a multitude of channel geometries and overall sample dimensions with quick turn-around.

Three components were cast in 3-D printed molds: the post, spacer, and main body of the device. The final version of the main body mold can be seen below in Figure 3-6. Early versions of the mold did not have the top shelf which resulted in many failed devices. The top shelf was added as an area to grip with tweezers when removing the cured PDMS from the mold. It was crucial to not make any contact with the bottom surface to keep it clean and not introduce any unwanted surface features such as gouges. Mold preparations were as follows:

1. Design the mold in SolidWorks and print on the 3-D printer
2. Clean support material from mold by scrubbing and pressure washing
3. De-gassing in an oven for roughly 2 hours at 80°C
4. Final pressure wash rinse and allow to air dry

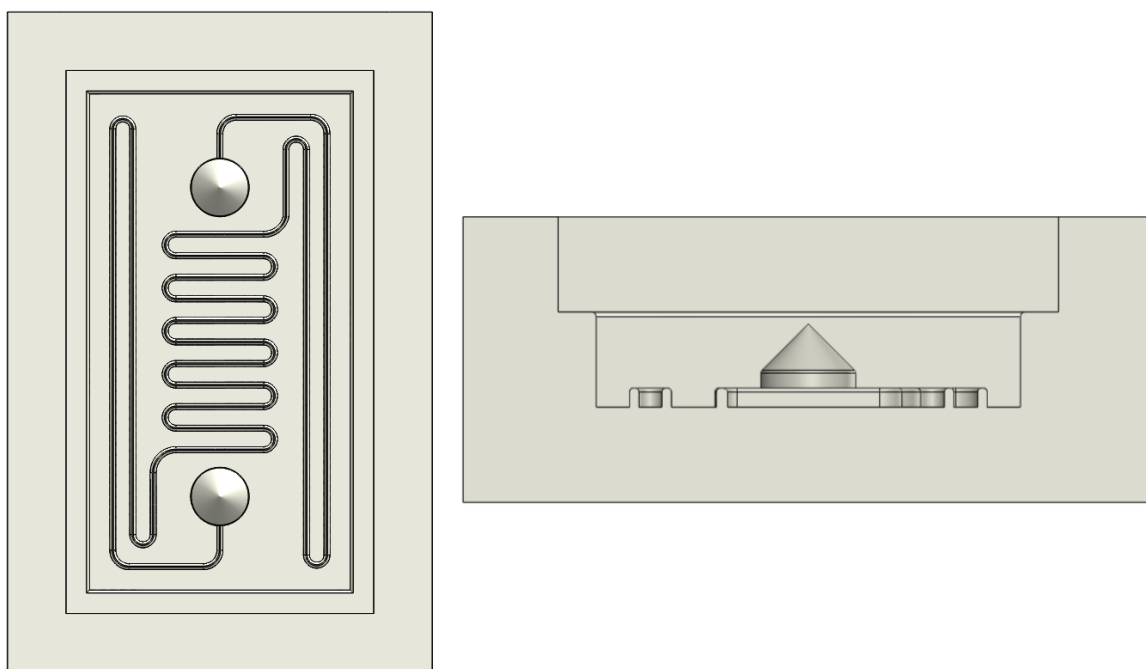


Figure 3-6: Left: Top view of the 3D printed mold. Right: Cross-sectional view of the mold showing the top shelf feature added to ensure a clean removal of the part to preserve the bonding surface.

Once a mold was ready to use, a 10:1 mixture of PDMS (Sylgard 184) was carefully poured in. A glass slide was scraped across the top to remove any excess material to ensure a level surface for later assembly. The mold would then be placed into a vacuum oven at room temperature for de-gassing, seen in Figure 3-7, removing any pockets of air in the PDMS resulting in a uniform consistency.



Figure 3-7: Left: 3D printed mold of micro channels. Right: De-gassing of the PDMS after casting is essential to ensure that no air bubbles are close to the channels.

Once level and de-gassed, the molds would be placed into the curing oven at 85°C for about 45 minutes, after which, would be removed and allowed to cool before removal of components from the mold. Upon removal, a 0.5 mm biopsy punch was used to complete the wells on the main body for electrodes and holes for threading the copper wires through on the spacer.

The sealing layer was made with the same 10:1 ratio PDMS and spin coated on a glass wafer to varying thicknesses from 200-1200 microns and cured in the oven for about 20

minutes at 85°C. The main body and the sealing layer were both exposed to corona discharge (Model BD-20 Electro-Technic Products, INC) roughly 30 seconds on each surface for attachment. Once attached, the assembly was placed on a hot plate at 45°C for 5 minutes, removed, and either left overnight or a for a few hours to ensure a mature bond.[61]

Once the assembly had time to settle, the sample was removed from the glass wafer by carefully cutting around the edge with a razor blade and slowly peeling it away. The removal process was the first test of the bond between the main body and the sealing layer. A sample that could detach from the glass wafer without delaminating would more than likely be robust enough for the task of repetitive testing. Common failures at this stage of peeling was inter-channel or edge delamination that resulted in shorting of the device or leaks, both causing a loss in resistance and a failed sample. Samples that did not delaminate during removal from the glass wafer and passed visual inspection would then be placed in an oven at 80°C along with a syringe and a petri dish full of LMPA (Roto117F/47C, 44.70% Bismuth, 5.30% Cadmium, 22.60% Lead, 8.30% Tin, and 19.10% Indium). The LMPA melts at 47°C and having the environment at 80°C allowed enough time with the oven door open for low pressure injection of the LMPA into the channels ensuring that no air bubbles were introduced and reducing unnecessary bulging of the channels that could potentially cause delamination. Once the channels were injected, copper electrodes coated in silver paste were inserted into the wells and the sample was removed from the oven and allowed to cool.

To ensure a flat surface for attachment to the post, the spacer block was attached. The spacer also acted as a support structure for the electrodes so they did not move under compression and possibly compromise the device by puncturing the sealing layer. The copper wire electrodes were then threaded through the side of the spacer block and the resistance of the device was checked. If the device had resistance, the wells of the spacer block would be filled with PDMS and cured sealing the sample, if not, the device would be placed back in the oven to melt the LMPA in an attempt to re-position the electrodes to form a complete circuit. Resistance was checked one last time before attaching to the bottom of the post with more PDMS concluding the fabrication process. An exploded view of the device is shown in Figure 3-8 followed by a 3D rendering seen in Figure 3-9.

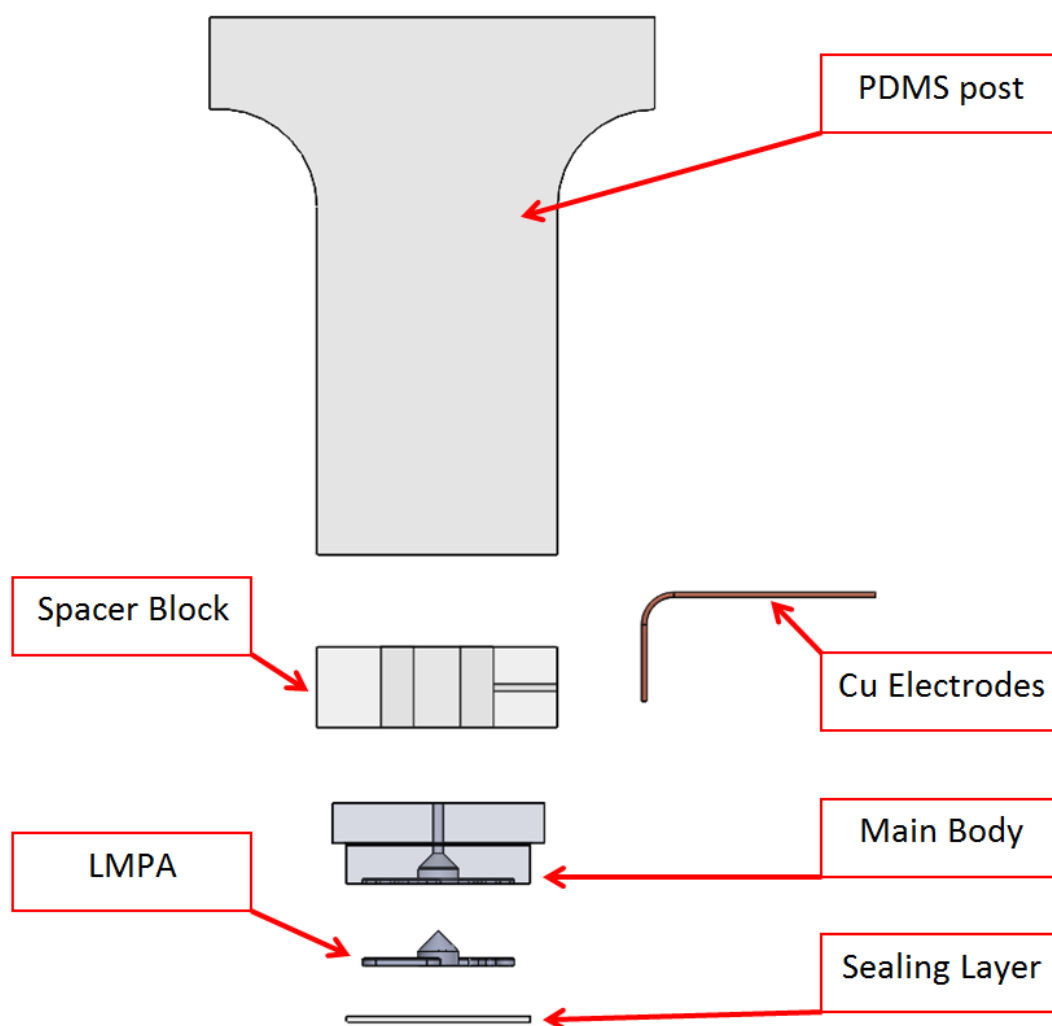


Figure 3-8: Exploded view of the final device. The sealing layer was attached via corona discharge. After the bond between the sealing layer and the main body matured, the channels were injected with LMPA while also inserting the electrodes. The spacer block was then attached with uncured PDMS and left to cure. Once the PDMS was cured and the spacer block secured in place, the electrodes were threaded through the side of the spacer block and the sample was sealed with more uncured PDMS before being attached to the post with uncured PDMS.

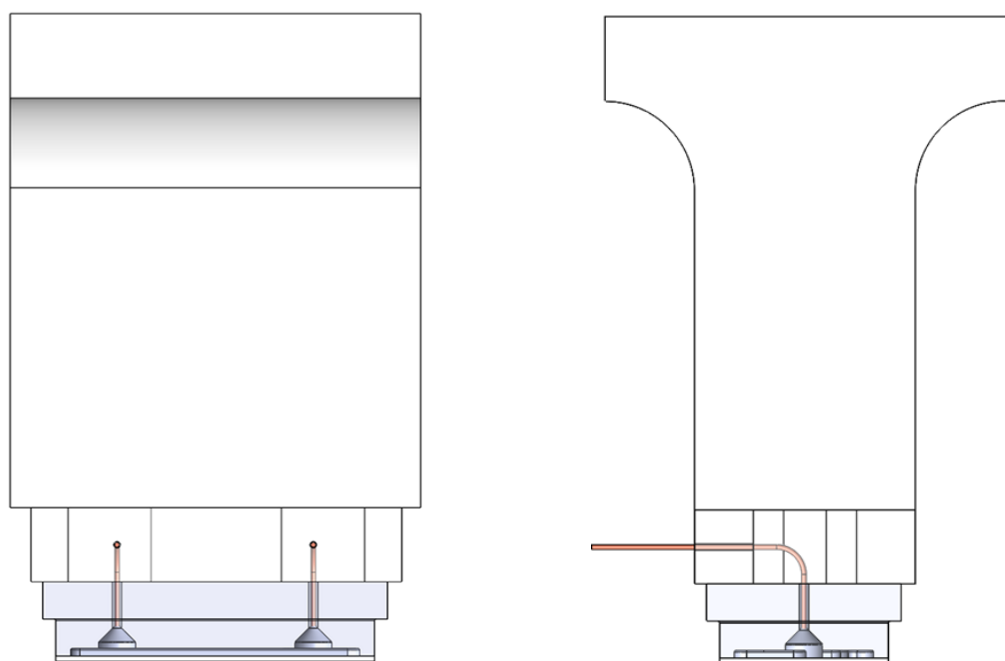


Figure 3-9: Left: Front side view of sample. Right: Side view of sample.

Chapter 4 – Testing Method and Setup

4.1 Introduction

To test for reversible tunable dry adhesion, a fixture to hold the devices was designed to be installed onto the Instron. Devices were then subjected to the four different test scenarios that were developed to differentiate the adhesion change between activated and un-activated states. To ensure activation and/or recognize failure of a device during testing, resistance was monitored continuously. If a device did lose resistance it was typically repairable assuming that no delamination or loss of material occurred. There was only one catastrophic failure during testing.

4.2 Experimental Setup

Testing of the devices was performed on an Instron 5969 with a 50 N load cell installed. A power supply (GW INSTEK GPR-30H100) was used for activation, and a digital multi-meter (ETEK CITY) to monitor the resistance. The PDMS post was inserted into the test fixture attached to the load cell side of the Instron while a glass slide (substrate) was installed on the bottom platform. The final testing setup can be seen below in Figures Figure 4-1 and Figure 4-2.

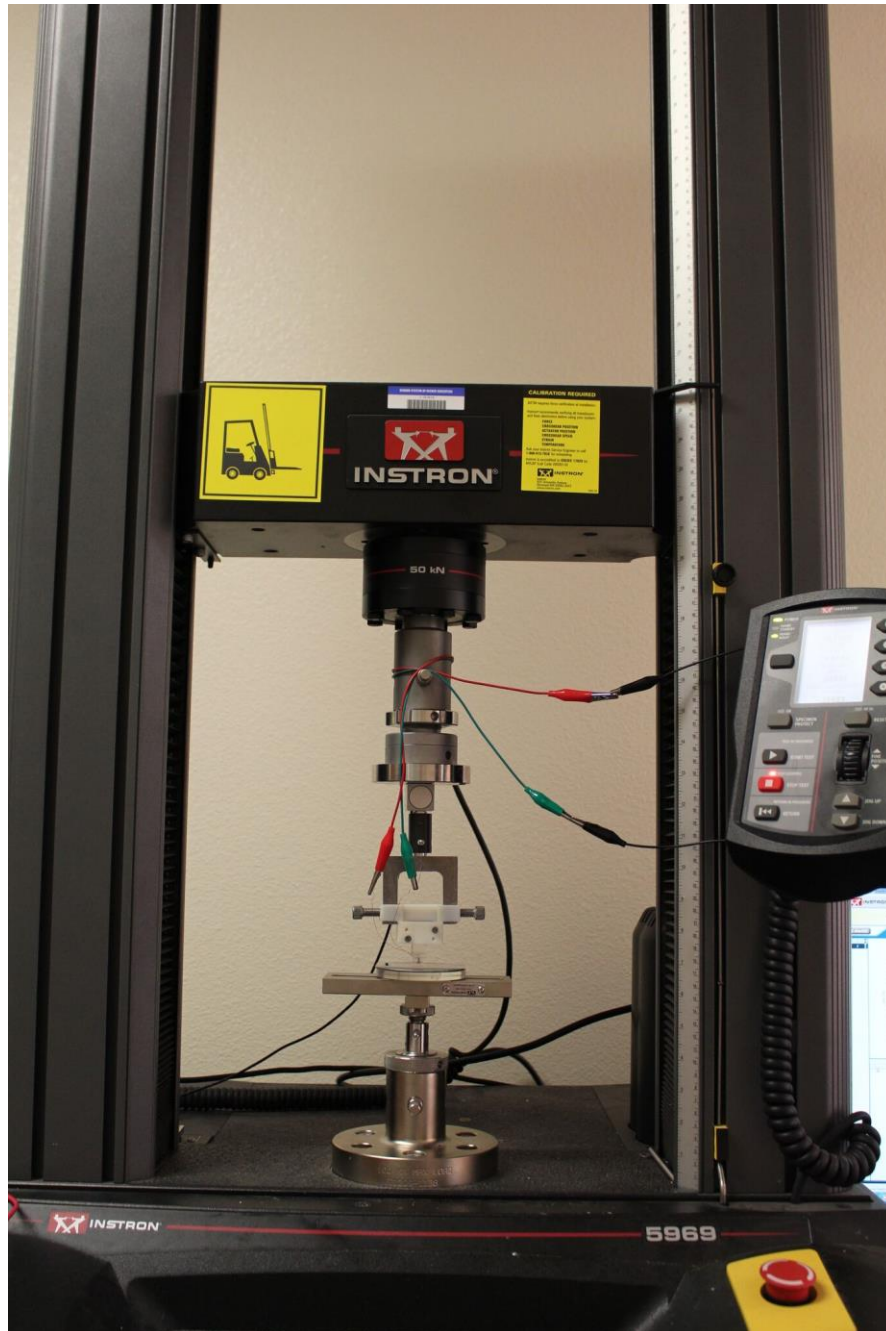


Figure 4-1: The experimental setup used for all the testing. A 50 N load cell was installed for more precise measuring.

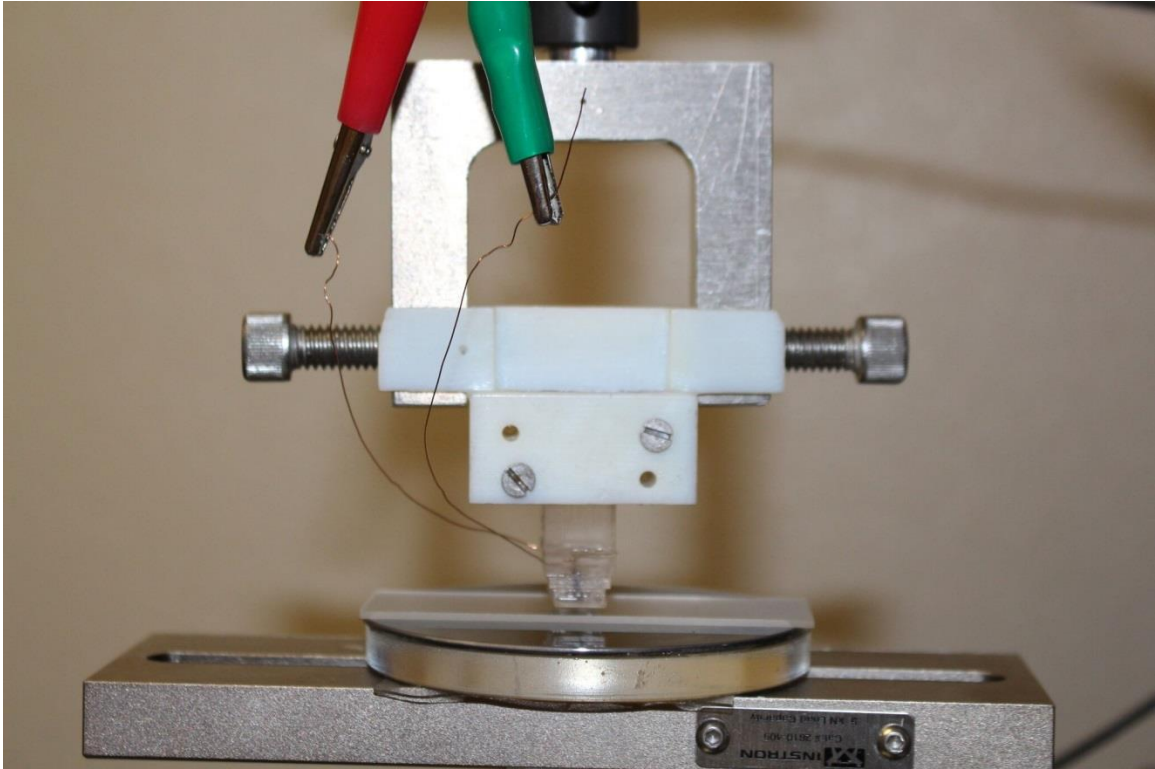


Figure 4-2: Close-up of the testing area showing exposed copper electrodes, fixed glass substrate, and fixture used to attach the post to the Instron.

Testing parameters for all samples were the same. A compressive preload of 14 N at a rate of $50 \frac{\mu m}{s}$ was applied to ensure that the entire surface of the device was in contact with the glass. This load was held for one minute before tension was applied at a rate of $100 \frac{\mu m}{s}$. At least four tests were conducted per condition. The first testing condition, Condition I, was a purely un-activated state and served as the baseline adhesion value for later tests. When a condition required activation and the test was completed, the sample was left to cool so that an un-activated test could be performed to ensure that the baseline adhesion values had not been affected to confirm reversibility.

4.3 Testing Issues

One of the main issues encountered throughout testing was loss of resistance which rendered samples useless as they could not be activated. Throughout the fabrication process resistance was checked every step because once the channels were sealed there was no way of altering them without partial destruction of the sample. Resistance loss commonly occurred during tests that called for activation and samples with thinner sealing layers. Repairable failures were typically those seen in Figure 4-3, that involve breaks in LMPA within the channels. To repair the samples, they were placed face down onto a glass surface on a hot plate at 65°C for 5 minutes. This process was repeated until resistance was re-gained, after which a baseline adhesion test would be performed to ensure the samples revival.

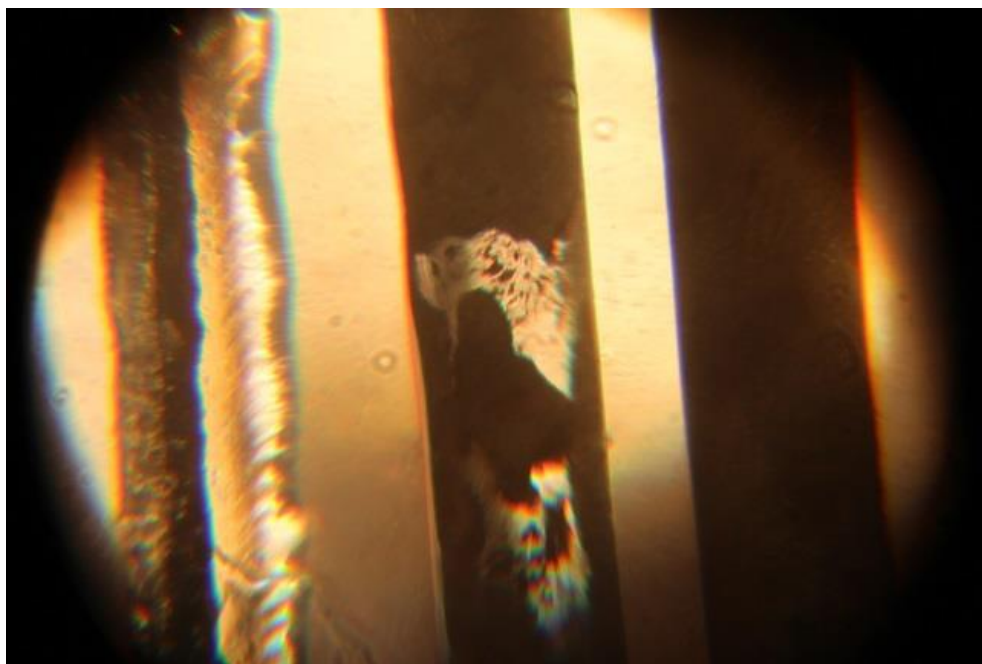


Figure 4-3: Picture taken under the microscope of a clear breakage in the LMPA channel that results in an un-usable sample as it cannot be activated. This type of break was repairable.



Figure 4-4: Left to Right: an un-tested sample. Same sample after testing showing the voids formed that resulted in a loss of resistance. After the repair process was performed, a baseline test was performed to confirm the adhesion value remained the same after repair.

There were un-repairable failures in earlier versions of the device most commonly involving the breach of a channel sidewall causing bleeding of LMPA into other channels short circuiting the sample, seen in Figure 4-5. Delamination or failure of the sealing layer was also un-repairable as it usually resulted in a loss of LMPA in the channel with no way of replacing of it. Although these types of failures were rare, one of the 400 μ m samples experienced a tear on the surface releasing LMPA. Really thin sealing layers were extremely susceptible to these failures as well, seen in Figure 4-6.

In the real application these soft grippers will be used to pick up an object, then activated with a higher voltage for a very short period of time (a pulse lasting one to two seconds) to drop the object. Since the gripper is under axial force for a very short time while the LMPA is in the liquid state, the probability of failure will greatly decrease. However, in the experiments a voltage has been applied for almost two minutes due to the specified low speed of the Instron cross head which increases the likelihood of creating voids and failures.

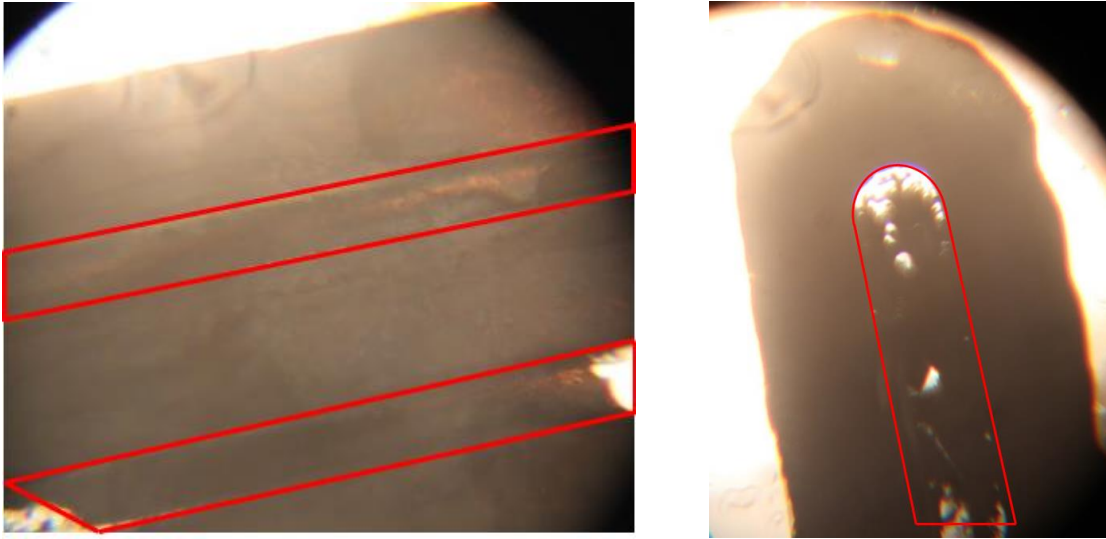


Figure 4-5: Images of breached sidewalls resulting in short circuiting of the sample. Areas within the red boxes are the spaces in between channels and should appear clear but instead are polluted with LMPA.



Figure 4-6: LMPA can be seen on the surface of the sample as a result of a failed sealing layer. Sealing layer thickness was roughly 100 μ m.

4.4 Testing Conditions

To study the device's capabilities three test conditions were generated. These conditions were designed to demonstrate the device's adhesion change abilities while guaranteeing that these changes were not a product of other scenarios, permanent or temporary, as to preserve reversibility. Although the numbering of the conditions does not correlate to the order in which they were performed, Condition I was always conducted first.

Condition I testing protocol, seen in Figure 4-7, was a “cold-cold” test, meaning that no activation occurred. This test served not only as the baseline for future tests, but was conducted after a sample was repaired, cleaned, or activated.

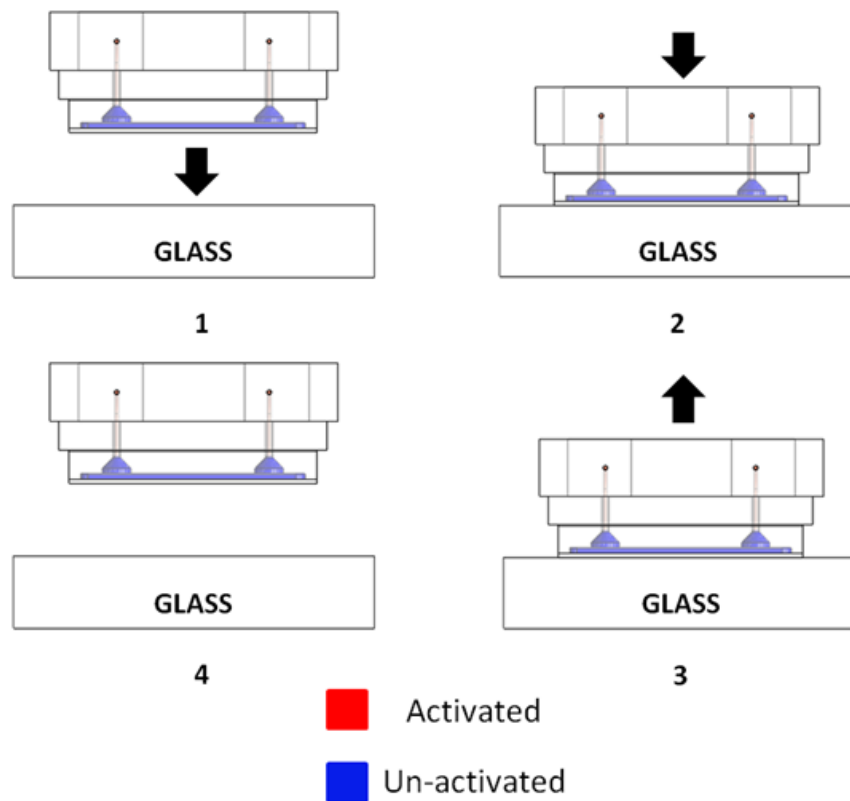


Figure 4-7: (1) Sample is brought into contact with glass surface. (2) Compressive preload of 14 N is held for 1 minute. (3) After 1 minute the tension is applied. (4) The sample loses contact with the glass surface concluding the test.

Condition II testing, Figure 4-8, was a “cold-hot” test and this is where the adhesion change capabilities would be seen. Successful devices would experience a reduction in adhesion from their baseline values. Many early iteration devices would fail during this test, typically liquid LMPA would leak out when the pre-load was applied. Commonly, when the material would soften it would push up higher into the electrode well, when the device was pulled away the material would remain there resulting in the breaks in the channels requiring repair.

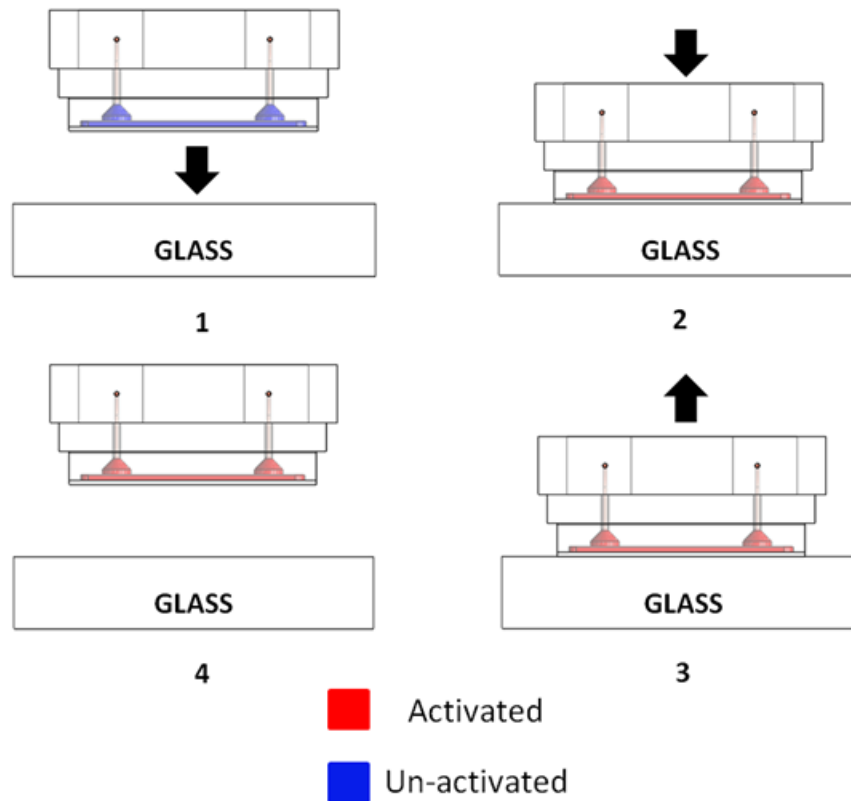


Figure 4-8: (1) Sample is brought into contact with glass surface. (2) Compressive preload of 14 N is applied for 1 minute with activation occurring in the last 30 seconds. (3) Tension is applied while the sample is still activated. (4) Sample loses contact with glass concluding the test.

Condition III testing, seen in Figure 4-9, was “hot-hot” meaning that the device was activated before initial contact and remained activated throughout the duration. This test pushed the boundaries of the robustness of the devices because any flaw in the sealing layer bonding would be exposed. The purpose of this test was to investigate the effects of activation to verify that adhesion change was due to activation and not factors such as surface contaminants.

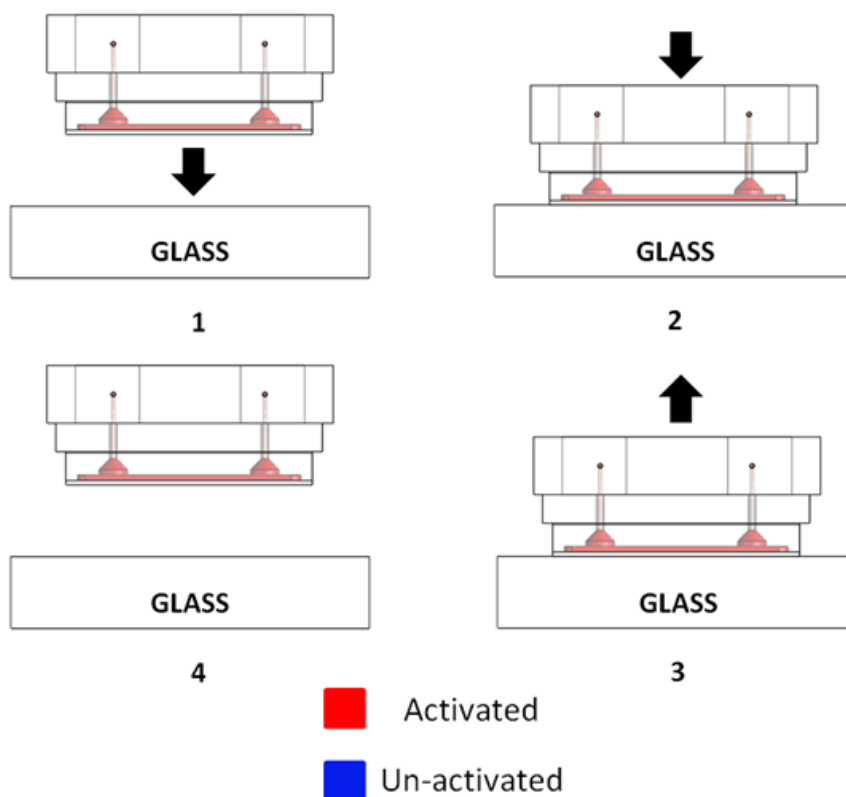


Figure 4-9: (1) Sample is activated and brought into contact with the glass. (2) Compressive preload of 14 N applied for 1 min. (3) Sample is pulled away from the surface. (4) Sample loses contact with glass surface concluding the test.

Chapter 5 – Results and Discussion

Introduction

Upon the first successfully fabricated and tested devices, simulations were run to learn more about where the crack would start and the effects of varying micro-channel height and sealing layer thicknesses on adhesion. The results of the simulation inspired the experiment to go beyond the initial goal of achieving tunable reversible dry adhesion and investigate a trend of adhesion values based off of dimension criterion, specifically, the sealing layer thickness. Condition I-III tests were conducted on A and B samples of specific sealing layer thicknesses and recorded. The results of both the simulations and experiment will be presented and discussed in this section.

5.1 Simulation Results

The success of the first devices defined the micro-channel pattern and overall dimensions (i.e. main body, post, and spacer block) of the future devices to be fabricated and tested leaving the micro-channel height and the sealing layer thickness as variable dimensions. However, it was not fully understood how the dimensions would affect the behavior of the device. Because of this, a 2-D quarter size model of a PDMS post with an embedded LMPA layer was simulated with varying sealing layer thickness (t) and LMPA layer heights (h).

First, the location of the crack would need to be known to best represent the system. The model was subjected to a tension force with no specified crack location. Multiple stress distribution plots of varying LMPA layer height and sealing layer thickness were generated under this model. Results showed that as the height of the LMPA layer gets

larger, the stress distribution maximum moved closer to the center, while the lower layers resulted in high stress concentrations closer to the edge signifying an edge crack formation.

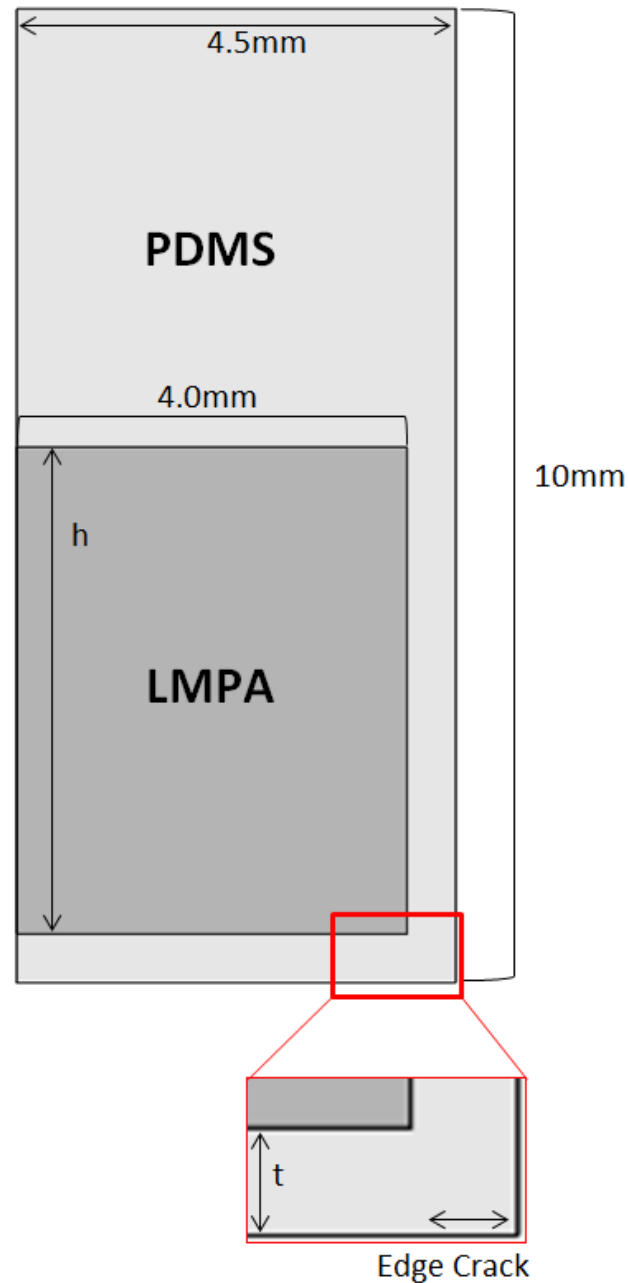


Figure 5-1: The simulations conducted were of a 2D quarter model of a LMPA core sample. Variables of the simulation were the height of the LMPA channel, h , and the thickness of the sealing layer, t .

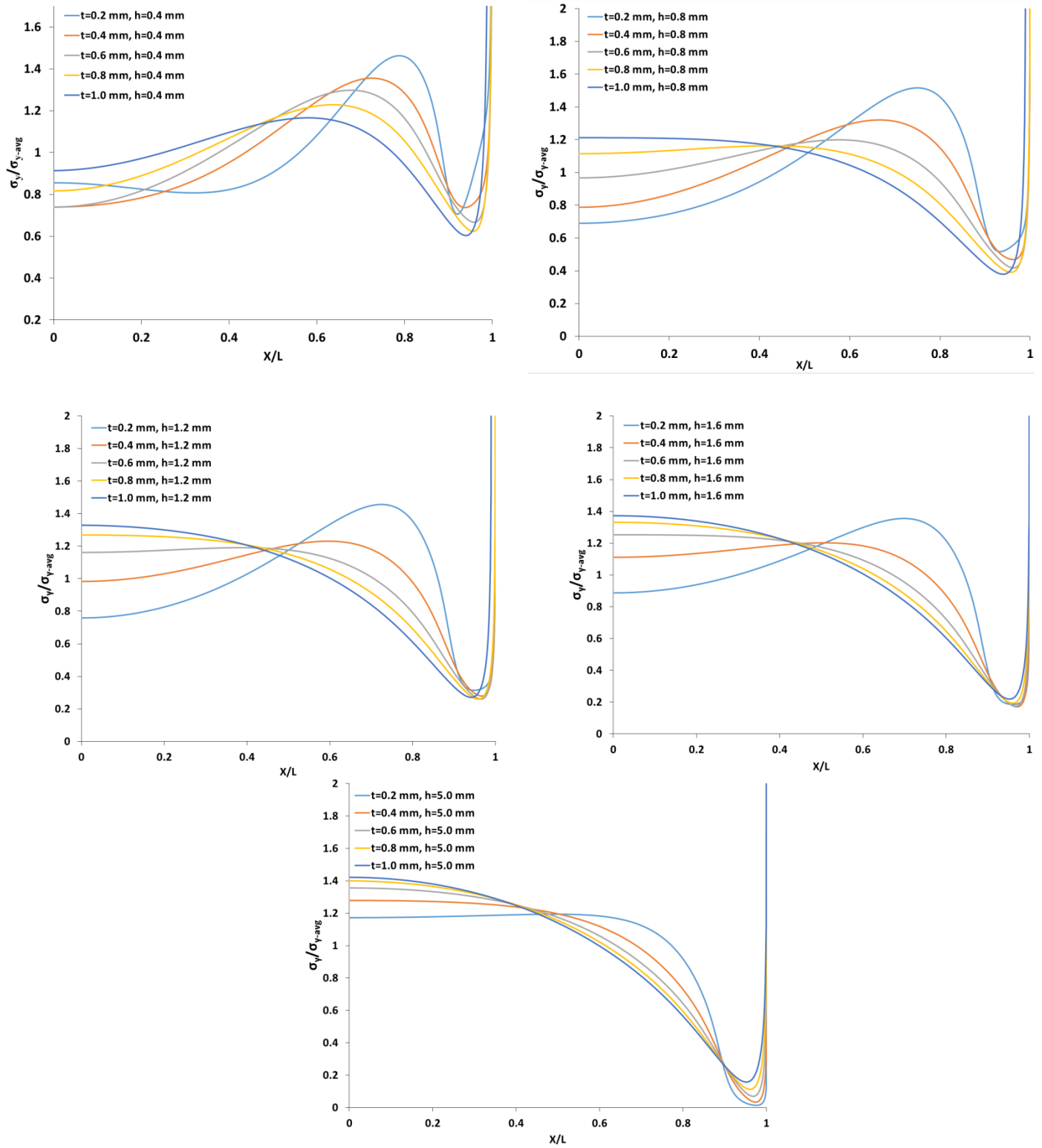


Figure 5-2: Shows the stress distributions for multiple LMPA layer and sealing layer thicknesses. Results show that for the tested system of $h=0.4$ mm the crack should begin on the edge. As the LMPA layer gets thicker, the crack location begins to move towards the center.

With this, an edge crack initiation was assumed and simulations were then ran to learn more about the LMPA and sealing layer thicknesses and their effects on the adhesion strength. A fixed displacement boundary condition was imposed on the adhered interface, while the interface between the PDMS and LMPA parts was modeled as perfectly bonded. Normal loading was applied by displacing the nodes along the top of the post in the z-direction; the displacement in x-y plane was free, which represents the fact that the post was held with a rigid fixture in the experiments.

The results of the simulation, shown by Figure 5-3, revealed that both the LMPA layer and the sealing layer thicknesses have an effect on strain energy and by proxy, the adhesion strength. More specifically, the devices fabricated for this experiment had a channel height of 400 μm with varying sealing layer thickness of 200 μm , 400 μm , 600 μm , 800 μm , and 1200 μm . FE simulations showed an expected maximum adhesion force with a sealing layer thickness of 600 μm for samples with LMPA layer thickness of 400 μm due to the least amount of strain energy being generated.

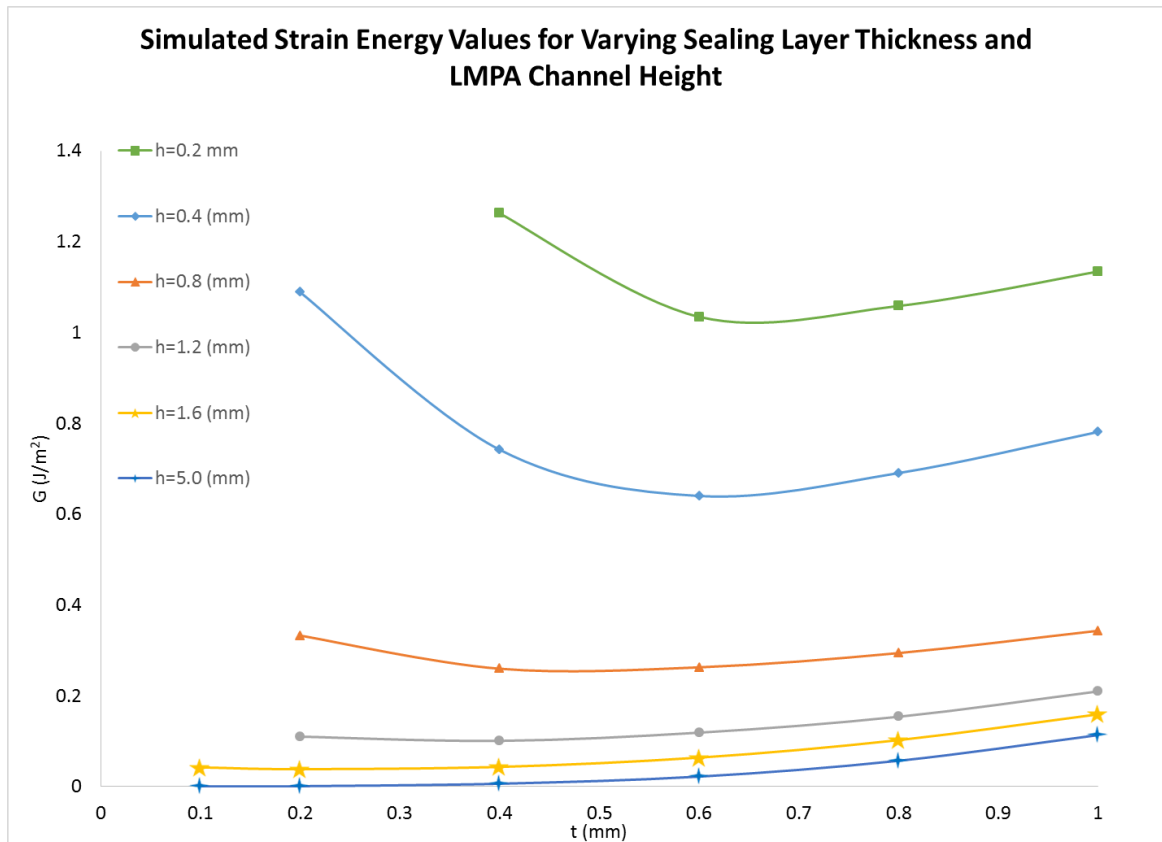


Figure 5-3: Results of the FEM simulations show that for the LMPA layer thickness of $400\mu\text{m}$, there should be a maximum adhesion value with a sealing layer thickness of $600\mu\text{m}$.

5.2 Experimental Results

One of the principal assumptions with the simulation versus the actual behavior of the device was no delamination between the PDMS and LMPA parts in the solid state (un-activated) and also no delamination between the post and the sealing layer, which could not be guaranteed. Corona Discharge was used to attach the PDMS sealing layer to the PDMS post which has the lowest PDMS-PDMS bonding strength of the available methods [62]. Bonding between the layers has the potential to fail under high adhesion forces and cause leaking of LMPA out of the channels which may have skewed the data.

Figure 5-4, Figure 5-5, and Figure 5-6 show the results of the three different testing conditions. Interestingly a maximum was observed at the predicted sealing layer thickness of 600 μm . Being that lower strain energy correlates to a higher adhesion force due to the prolonged crack initiation, the data appears to have followed the trend predicted by the simulation. However, with the adhesion of the last two samples, 800 μm and 1200 μm , being lower than the first two, 200 μm and 400 μm , a deviation from predicted trend occurred. This discrepancy could be explained by the assumption of perfect bonding at all interfaces in the FE simulations while delamination is likely to occur at the PDMS-PDMS interface of some samples due to weak bonding.

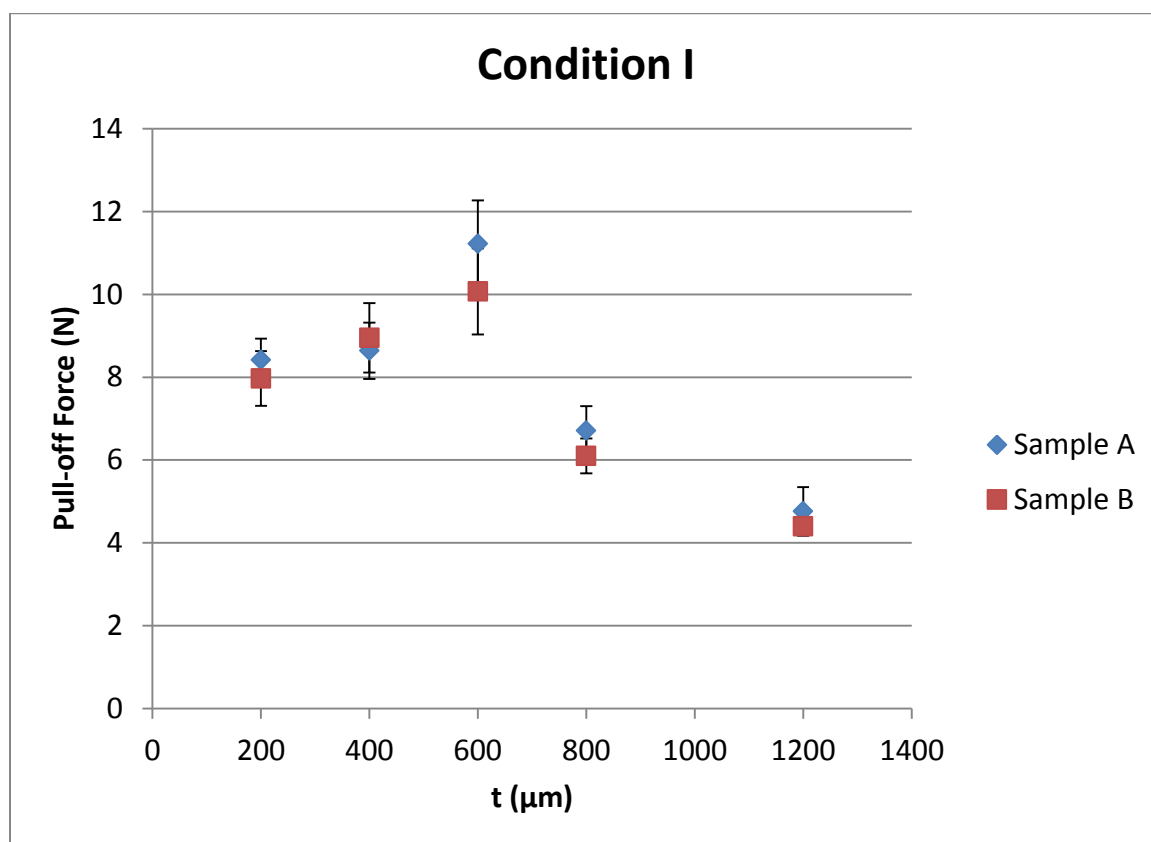


Figure 5-4: Condition I results show a maximum baseline adhesion value associated with the 600μm sealing layer thickness as predicted by the FE simulation. Other data follows the behavioral trend but deviates possibly due to delamination effects. Error bars correlate to the standard deviation.

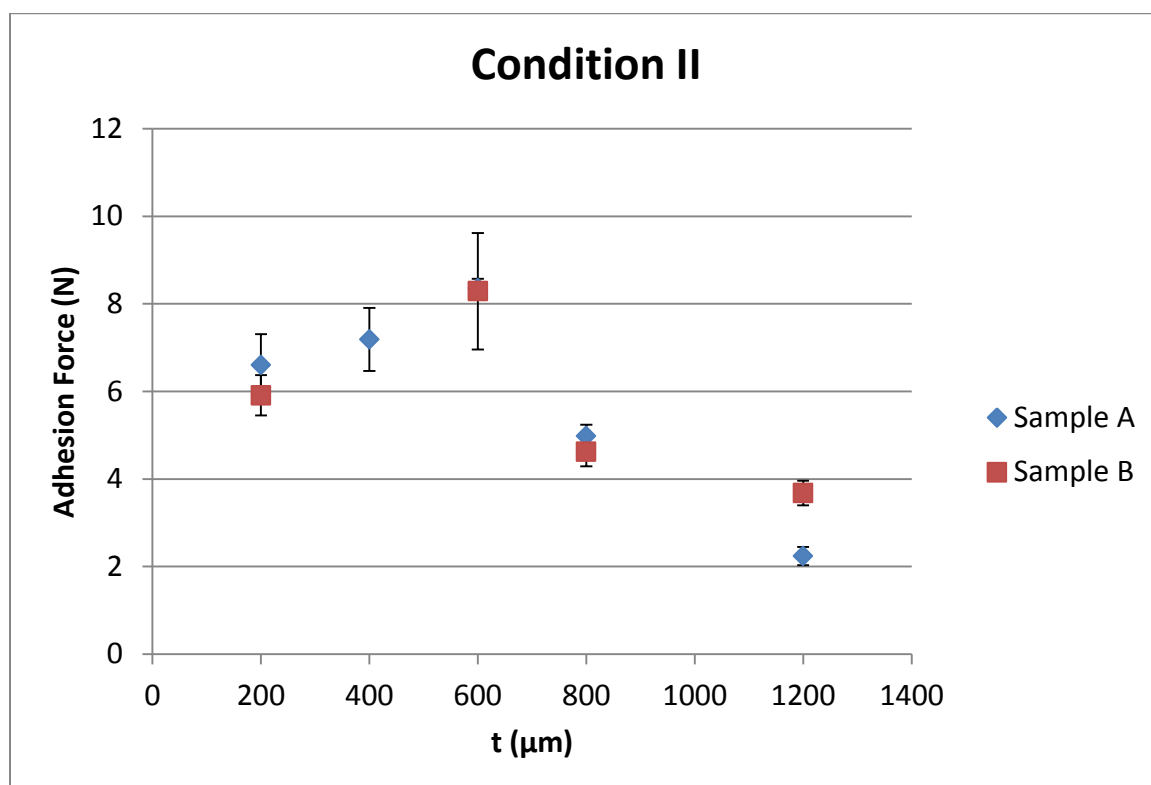


Figure 5-5: Condition II results show the same simulation trend with a maximum at 600 μm sealing layer. One of the samples from the 400 μm sealing layer thickness batch catastrophically failed during this test.

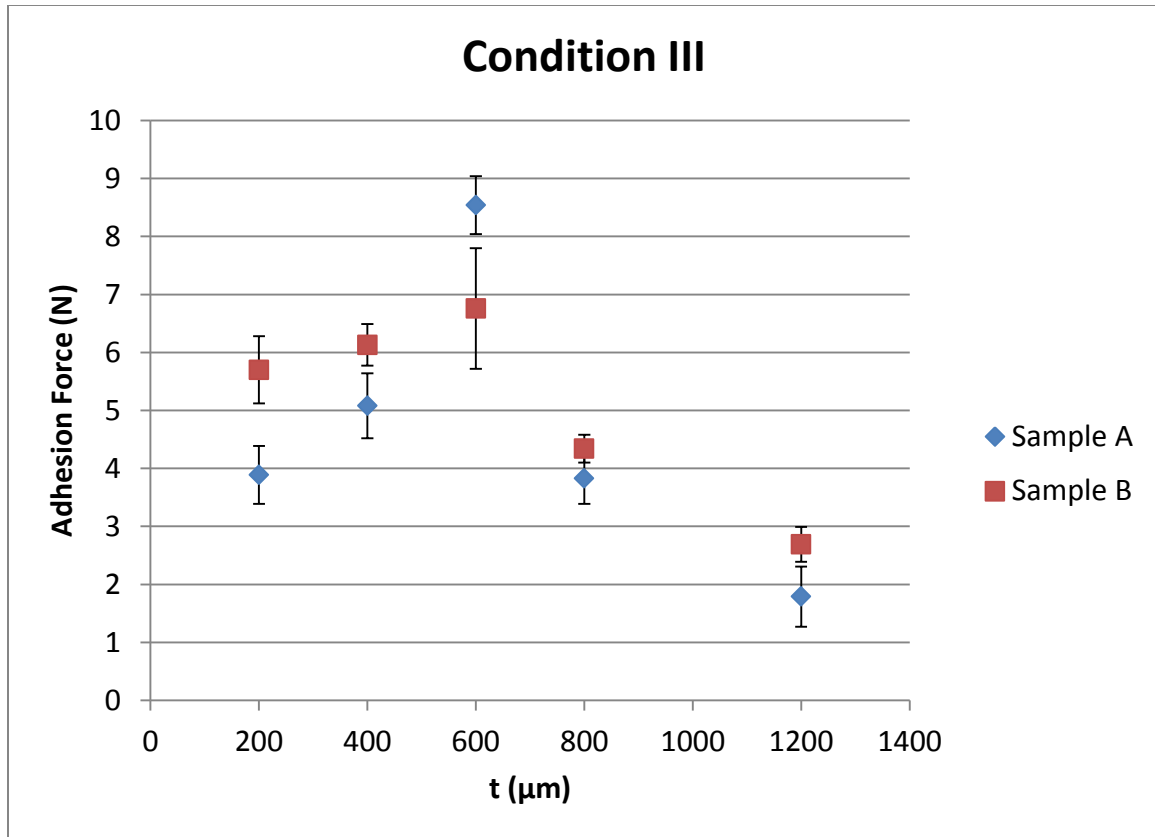


Figure 5-6: Condition III was performed to investigate the effect an initial un-activated surface contact versus an activated initial surface contact. The resulting adhesions forces were slightly lower than those of an initial un-activated surface contact.

The tunable adhesion capabilities of the devices were determined by the ratio of Condition I and Condition II results. These results of the adhesion change, seen in Figure 5-7, stayed rather constant for all sealing layer thicknesses being the highest for the 1.2 mm samples at 1.66. Interestingly the ratio of Condition I and Condition III was a higher adhesion change, but was not investigated in the experiment.

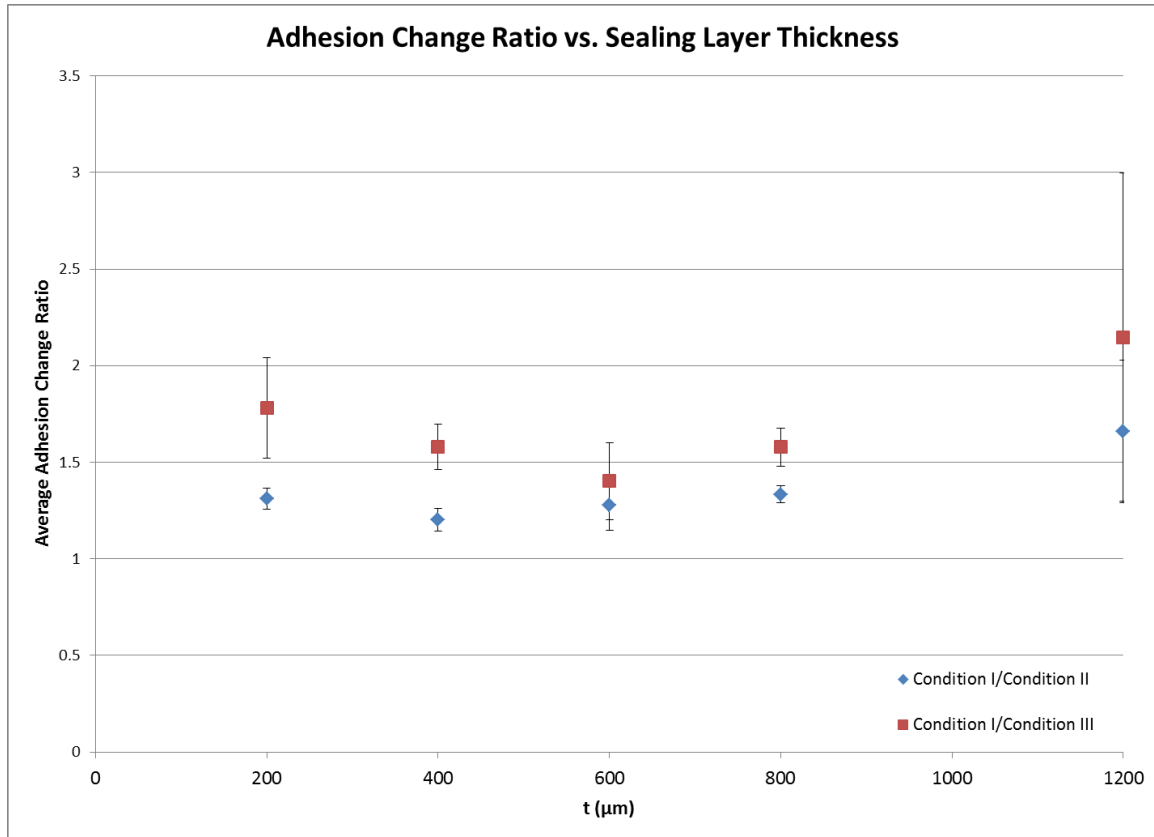


Figure 5-7: Comparing the adhesion change ratio of Condition I/Condition II and Condition I/Condition III.

To display the adhesion change capabilities of the device, a demo was conducted using the 600 μm A sample. A piece of glass was attached to an aluminum weight of 4.46 N to ensure similar surface contact as that of the experiments. The demo first followed Condition I protocol to obtain a baseline adhesion time that resulted in a total of 22 seconds before the weight was released naturally. The demo then followed Condition II protocol to see if the tunable adhesion could be observed. The weight was picked up and held for approximately six seconds before applying 5.5 volts, activating the sample and releasing the weight in less than two seconds.

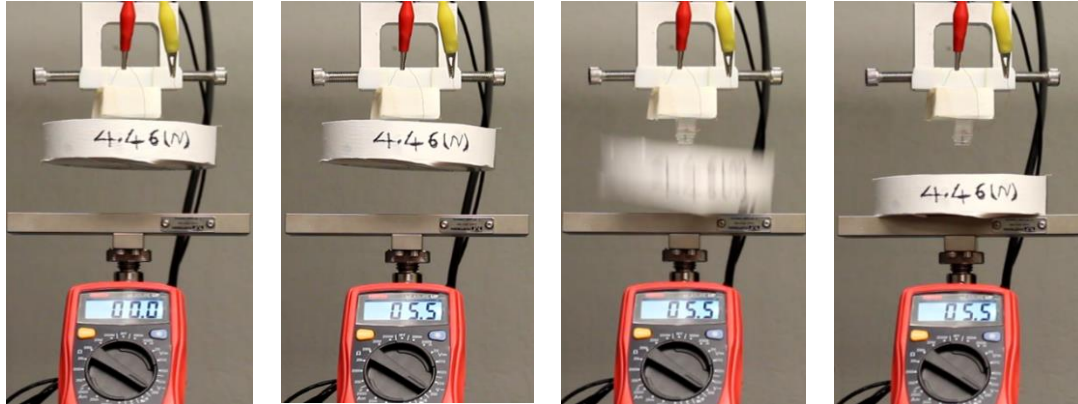


Figure 5-8: Left to Right: frames taken from the demo video show the device holding the 4.46 N weight for approximately six seconds before the device is activated dropping the weight in less than two seconds. The multi-meter shows when the device was activated with 5.5 volts.

5.3 Discussion

During testing, sample B of the 400 μm experienced a tear on the surface of the sealing layer resulting in material loss and ultimately a catastrophic failure. This was the only sample to fail of such events, although many samples had to be repaired on the hotplate throughout testing. This was more common in the samples with thinner sealing layers than in the samples with thicker sealing layers.

The experimental data followed the trend of the simulation results but did deviate, possibly due to uncontrollable delamination factors. Fabrication tools and methods may have allowed for unreliable bonding between two PDMS layers causing the discrepancy. The simulations were performed with the assumption that no delamination was occurring, but could not be guaranteed. Figure 5-9 shows a summary of the results for the three conditions.

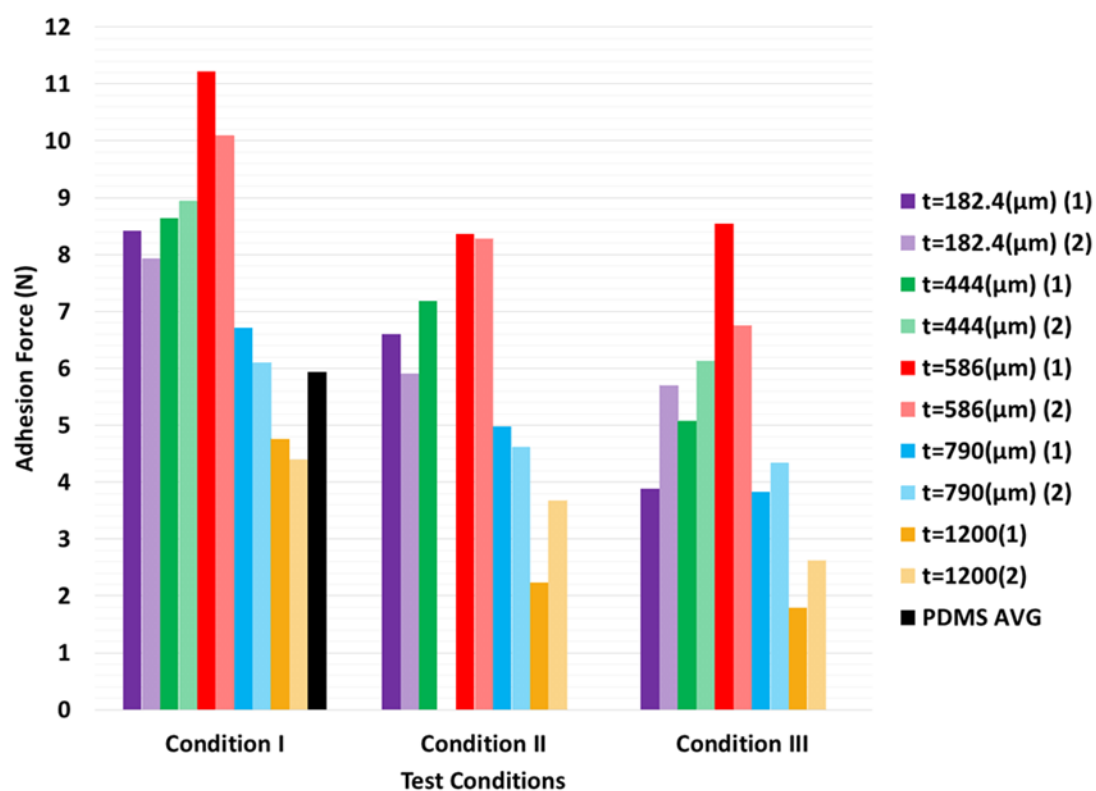


Figure 5-9: Summary of the adhesion data for A and B samples. A maximum adhesion force seen at 600 μm sealing layer thickness is consistent with FE simulations.

Chapter 6 – Summary, Conclusions, and Future Work

6.1 Summary

The goal of the experiment was to show tunable reversible dry adhesion. Stress and strain distributions were manipulated by a stiffness tunable layer that could mitigate stress concentration to increase adhesion forces. Design of the device took much iteration, but with the use of a 3D printer alterations could be made quickly allowing the project to stay on schedule. The final version of the devices had micro channels 200 μm wide and 400 μm tall with a channel spacing of 500 μm . Overall contact surface of the device was 9.12 mm by 17.17 mm with the channels 700 μm away from the edges.

Molds for the post, spacer block, and main body were made with a 3D printer and sealing layers were made on a glass disk with a spin coater. Corona discharge was implemented to bond the sealing layer to the main body before LMPA was injected into the channels. Spacer blocks were attached with uncured PDMS and copper electrodes were inserted into the wells and threaded through the side wall of the spacer block before the wells were sealed with PDMS. Successful devices had a resistance of approximately 2 Ohms.

FEM simulations for varying LMPA micro channel heights and sealing layer thicknesses were conducted before testing. Results of the FEM showed that as the LMPA layer becomes thicker the crack location moves to the center of the device rather than the edge because of higher stress values. Results also show that there is a relationship between the LMPA micro channel height and sealing layer thickness predicting a maximum adhesion

value for the sample with LMPA channels 400 μm tall and a sealing layer thickness of 600 μm .

An Instron testing machine was outfitted with a fixture on top that would hold the devices and a glass substrate installed on the bottom to ensure a smooth surface for testing. Devices were hooked up to a power supply for activation and subjected to three different testing conditions with only one device failing during the extensive testing.

6.2 Conclusions

This thesis is concerned with a novel elastomeric gripper with tunable reversible dry adhesion. Average adhesion change capabilities of 1.36 times due to the manipulation of the mechanical stiffness of LMPA-filled channels embedded in a PDMS post are shown. These LMPA thin strips can soften upon the application of voltage, which results in less uniform stress distribution on the adhered interface, and thus reduction of the adhesion strength. Reversibility has been shown by performing baseline tests after all tests requiring activation to rule out any loss of adhesion due to heat, surface contaminants, or device failure.

Test results and FEM simulations agree on a relationship between the dry adhesion and the distance from the LMPA channels to the contact surface (i.e. sealing layer thickness), and share a maximum adhesion value for devices with 600 μm sealing layers at about 11 N. This device demonstrated its low power adhesion change capabilities by releasing a weight (previously held for 22 seconds) within two seconds of activation with an applied voltage of 5.5 V and a power consumption of about 7.56 W. With improvement, the

tunable reversible dry adhesive devices based on mechanisms illustrated here will be a reliable handling option for industry and research in the future.

6.3 Future Work

The first aspect of the devices that needs to be improved is the fabrication process, specifically the bonding process between the sealing layer and the main body. A procedure that could guarantee bonding with no delamination between the two parts might reduce the discrepancy between the experimental results and the simulation results. An improved bonding process would also allow for more dimensional combinations to be experimented with. One of the reasons that the channel pattern and geometry were chosen was the consideration of being compatible with the bonding process. Having the opportunity to experiment with different channel patterns and distances from the channels to the edge of the sample could increase adhesion change ratio.

Secondly, the assembly process needs to be improved. The lack of keying holes or assembly fixtures led to some misaligned and/or non-planar devices. Having the correct tools and geometrical features to properly align and secure the devices during curing would result in more consistent batches of samples and results.

Lastly, the processes of fabrication and experimentation should be more controlled to provide better accuracy in results and increase uniformity of devices. For example, fabrication steps that require exposure to heat, such as curing and LMPA injection, need to be consistent in not only temperature but time as well. Furthermore, the testing environment needs to be monitored (values such as relative humidity or ambient

temperature) to aid in ruling out possible environmental factors that may influence a device's adhesive capabilities.

With optimal fabrication and assembly methods, the devices could be manufactured large scale for assembly lines or custom fabricated for specific handling tasks. Re-tooling a manufacturing line could require less time and be made cheaper and simpler. With no need for excess lines, such as pneumatic, to function, and only requiring simple circuitry for activation, these devices would be ideal for manufacturing plants looking to reduce equipment complexity and power usage.

The ability to quickly change adhesion capabilities would be ideal for human and robot wall climbing systems. Fabrication of custom units with objective-specific lightweight designs only requiring simple circuitry would be very conducive to increasing speed and efficiency of the climber. Devices can be made into a plethora of shapes and sizes to fit the needs of any gripping tasks. Tunable reversible dry adhesion is a clean, minimalistic approach that with development could replace bulky traditional methods.

References

- [1] Majidi, C., 2014, "Soft robotics: a perspective—current trends and prospects for the future," *Soft Robotics*, 1(1), pp. 5-11.
- [2] Fantoni, G., Santochi, M., Dini, G., Tracht, K., Scholz-Reiter, B., Fleischer, J., Kristoffer Lien, T., Seliger, G., Reinhart, G., Franke, J., Nørgaard Hansen, H., and Verl, A., 2014, "Grasping devices and methods in automated production processes," *CIRP Annals - Manufacturing Technology*, 63(2), pp. 679-701.
- [3] Tai, K., El-Sayed, A.-R., Shahriari, M., Biglarbegian, M., and Mahmud, S., 2016, "State of the Art Robotic Grippers and Applications," *Robotics*, 5(2), p. 11.
- [4] McKenzie, R. M., Barraclough, T. W., and Stokes, A. A., 2017, "Integrating Soft Robotics with ROS-A hybrid pick and place arm," *arXiv preprint arXiv:1702.00694*.
- [5] Li, Y., Chen, Y., Yang, Y., and Wei, Y., 2017, "Passive Particle Jamming and Its Stiffening of Soft Robotic Grippers," *IEEE Transactions on Robotics*, PP(99), pp. 1-10.
- [6] Krahn, J., Fabbro, F., and Menon, C., 2017, "A Soft-Touch Gripper for Grasping Delicate Objects," *IEEE/ASME Transactions on Mechatronics*, PP(99), pp. 1-1.
- [7] Song, S., Majidi, C., and Sitti, M., "GeckoGripper: A soft, inflatable robotic gripper using gecko-inspired elastomer micro-fiber adhesives," *Proc. 2014 IEEE/RSJ International Conference on Intelligent Robots and Systems*, pp. 4624-4629.
- [8] Shintake, J., Rosset, S., Schubert, B., Floreano, D., and Shea, H., 2016, "Versatile soft grippers with intrinsic electroadhesion based on multifunctional polymer actuators," *Advanced Materials*, 28(2), pp. 231-238.
- [9] Mohammadi Nasab, A., Sabzehzar, A., Tatari, M., Majidi, C., and Shan, W., 2017, "A Soft Gripper with Rigidity Tunable Elastomer Strips as Ligaments," *Soft Robotics*.
- [10] Shan, W., Diller, S., Tutcuoglu, A., and Majidi, C., 2015, "Rigidity-tuning conductive elastomer," *Smart Materials and Structures*, 24(6), p. 065001.
- [11] Hao, Y., Gong, Z., Xie, Z., Guan, S., Yang, X., Ren, Z., Wang, T., and Wen, L., "Universal soft pneumatic robotic gripper with variable effective length," *Proc. 2016 35th Chinese Control Conference (CCC)*, pp. 6109-6114.
- [12] Crooks, W., Vukasin, G., O'Sullivan, M., Messner, W., and Rogers, C., 2016, "Fin Ray Effect Inspired Soft Robotic Gripper: From the RoboSoft Grand Challenge Toward Optimization," *Frontiers in Robotics and AI*, 3, p. 70.
- [13] Plante, J.-S., and Dubowsky, S., 2006, "Large-scale failure modes of dielectric elastomer actuators," *International Journal of Solids and Structures*, 43(25–26), pp. 7727-7751.
- [14] Duduta, M., Wood, R. J., and Clarke, D. R., 2016, "Multilayer Dielectric Elastomers for Fast, Programmable Actuation without Prestretch," *Advanced Materials*, 28(36), pp. 8058-8063.
- [15] Poulin, A., Rosset, S., and Shea, H. R., 2015, "Printing low-voltage dielectric elastomer actuators," *Applied Physics Letters*, 107(24), p. 244104.
- [16] Shaeffer, D. K., 2013, "MEMS inertial sensors: A tutorial overview," *IEEE Communications Magazine*, 51(4), pp. 100-109.

- [17] Bock, K., Feil, M., and Landesberger, C., 2013, "Thinning, Dicing, Handling and Assembly Processes for Thin Chips built an Integrated Approach," *Foldable Flex and Thinned Silicon Multichip Packaging Technology*, 1, p. 101.
- [18] Bou, S. C., Almansa, A., Balabanava, N., and Rymuza, Z., 2005, "Handling processes in microsystems technology," *Proc. of IEEE/ASME AIM*, Monterey, USA.
- [19] O'Neal, C. B., Malshe, A. P., Singh, S. B., Brown, W., and Eaton, W., "Challenges in the packaging of MEMS," *Proc. Advanced Packaging Materials: Processes, Properties and Interfaces*, 1999. Proceedings. International Symposium on, IEEE, pp. 41-47.
- [20] Meitl, M. A., Zhu, Z.-T., Kumar, V., Lee, K. J., Feng, X., Huang, Y. Y., Adesida, I., Nuzzo, R. G., and Rogers, J. A., 2006, "Transfer printing by kinetic control of adhesion to an elastomeric stamp," *Nat Mater*, 5(1), pp. 33-38.
- [21] Feng, X., Meitl, M. A., Bowen, A. M., Huang, Y., Nuzzo, R. G., and Rogers, J. A., 2007, "Competing fracture in kinetically controlled transfer printing," *Langmuir*, 23(25), pp. 12555-12560.
- [22] Eisenhaure, J. D., Rhee, S. I., Ala'a, M., Carlson, A., Ferreira, P. M., and Kim, S., 2016, "The use of shape memory polymers for MEMS assembly," *Journal of Microelectromechanical Systems*, 25(1), pp. 69-77.
- [23] Huang, Y., Zheng, N., Cheng, Z., Chen, Y., Lu, B., Xie, T., and Feng, X., 2016, "Direct Laser Writing-Based Programmable Transfer Printing via Bioinspired Shape Memory Reversible Adhesive," *ACS Applied Materials & Interfaces*, 8(51), pp. 35628-35633.
- [24] Eisenhaure, J., and Kim, S. C., 2016, "Laser-Driven Shape Memory Effect for Transfer Printing Combining Parallelism with Individual Object Control," *Advanced Materials Technologies*, 1(7), pp. 1600098-n/a.
- [25] Carlson, A., Kim-Lee, H.-J., Wu, J., Elvikis, P., Cheng, H., Kovalsky, A., Elgan, S., Yu, Q., Ferreira, P. M., and Huang, Y., 2011, "Shear-enhanced adhesiveless transfer printing for use in deterministic materials assembly," *Applied Physics Letters*, 98(26), p. 264104.
- [26] Xia, Y., Qin, D., and Whitesides, G. M., 1996, "Microcontact printing with a cylindrical rolling stamp: A practical step toward automatic manufacturing of patterns with submicrometer-sized features," *Advanced Materials*, 8(12), pp. 1015-1017.
- [27] Choi, M., Jang, B., Lee, W., Lee, S., Kim, T. W., Lee, H.-J., Kim, J.-H., and Ahn, J.-H. C., 2017, "Stretchable Active Matrix Inorganic Light-Emitting Diode Display Enabled by Overlay-Aligned Roll-Transfer Printing," *Advanced Functional Materials*, pp. 1606005-n/a.
- [28] Yi, H., Hwang, I., Sung, M., Lee, D., Kim, J.-H., Kang, S. M., Bae, W.-G., and Jeong, H. E., 2014, "Bio-inspired adhesive systems for next-generation green manufacturing," *International Journal of Precision Engineering and Manufacturing-Green Technology*, 1(4), pp. 347-351.
- [29] Dzyaloshinskii, I. E. e., Lifshitz, E., and Pitaevskii, L. P., 1961, "General theory of Van Der Waals' forces," *Physics-Uspekhi*, 4(2), pp. 153-176.
- [30] Autumn, K., and Peattie, A. M., 2002, "Mechanisms of Adhesion in Geckos1," *Integrative and Comparative Biology*, 42(6), pp. 1081-1090.
- [31] Autumn, K., Sitti, M., Liang, Y. A., Peattie, A. M., Hansen, W. R., Sponberg, S., Kenny, T. W., Fearing, R., Israelachvili, J. N., and Full, R. J., 2002, "Evidence for van

der Waals adhesion in gecko setae," *Proceedings of the National Academy of Sciences*, 99(19), pp. 12252-12256.

[32] Sitti, M., and Fearing, R. S., 2003, "Synthetic gecko foot-hair micro/nano-structures as dry adhesives," *Journal of Adhesion Science & Technology*, 17(8), pp. 1055-1073.

[33] Autumn, K., Liang, Y. A., Hsieh, S. T., Zesch, W., Chan, W. P., Kenny, T. W., Fearing, R., and Full, R. J., 2000, "Adhesive force of a single gecko foot-hair," *Nature*, 405(6787), pp. 681-685.

[34] Zhou, M., Pesika, N., Zeng, H., Tian, Y., and Israelachvili, J., 2013, "Recent advances in gecko adhesion and friction mechanisms and development of gecko-inspired dry adhesive surfaces," *Friction*, 1(2), pp. 114-129.

[35] Brodoceanu, D., Bauer, C., Kroner, E., Arzt, E., and Kraus, T., 2016, "Hierarchical bioinspired adhesive surfaces—a review," *Bioinspiration & Biomimetics*, 11(5), p. 051001.

[36] Rong, Z., Zhou, Y., Chen, B., Robertson, J., Federle, W., Hofmann, S., Steiner, U., and Goldberg-Oppeneheimer, P., 2014, "Bio-Inspired Hierarchical Polymer Fiber–Carbon Nanotube Adhesives," *Advanced Materials*, 26(9), pp. 1456-1461.

[37] Lee, J., Bush, B., Maboudian, R., and Fearing, R. S., 2009, "Gecko-Inspired Combined Lamellar and Nanofibrillar Array for Adhesion on Nonplanar Surface," *Langmuir*, 25(21), pp. 12449-12453.

[38] Lee, H., Um, D.-S., Lee, Y., Lim, S., Kim, H.-j., and Ko, H., 2016, "Octopus-Inspired Smart Adhesive Pads for Transfer Printing of Semiconducting Nanomembranes," *Advanced Materials*, 28(34), pp. 7457-7465.

[39] Kasem, H., Tsipenyuk, A., and Varenberg, M., 2015, "Biomimetic wall-shaped hierarchical microstructure for gecko-like attachment," *Soft matter*, 11(15), pp. 2909-2915.

[40] Chen, R., 2015, "A Gecko-Inspired Electroadhesive Wall-Climbing Robot," *IEEE Potentials*, 34(2), pp. 15-19.

[41] Zhang, Y., Wu, X., and Mei, T., "Design and experiment of a tank-like wall-climbing robot using fibril dry adhesives," *Proc. 2016 IEEE International Conference on Mechatronics and Automation*, pp. 671-676.

[42] Li, Y., Krahn, J., and Menon, C., 2016, "Bioinspired Dry Adhesive Materials and Their Application in Robotics: A Review," *Journal of Bionic Engineering*, 13(2), pp. 181-199.

[43] Kim, S., Spenko, M., Trujillo, S., Heyneman, B., Santos, D., and Cutkosky, M. R., 2008, "Smooth Vertical Surface Climbing With Directional Adhesion," *IEEE Transactions on Robotics*, 24(1), pp. 65-74.

[44] Murphy, M. P., Kute, C., Mengüç, Y., and Sitti, M., 2011, "Waalbot II: Adhesion Recovery and Improved Performance of a Climbing Robot using Fibrillar Adhesives," *The International Journal of Robotics Research*, 30(1), pp. 118-133.

[45] Krahn, J., Liu, Y., Sadeghi, A., and Menon, C., 2011, "A tailless timing belt climbing platform utilizing dry adhesives with mushroomcaps," *Smart Materials and Structures*, 20(11), p. 115021.

[46] Hawkes, E. W., Eason, E. V., Christensen, D. L., and Cutkosky, M. R., 2015, "Human climbing with efficiently scaled gecko-inspired dry adhesives," *Journal of The Royal Society Interface*, 12(102).

- [47] Drotleff, D.-M., Blümmler, P., and del Campo, A., 2014, "Magnetically Actuated Patterns for Bioinspired Reversible Adhesion (Dry and Wet)," *Advanced Materials*, 26(5), pp. 775-779.
- [48] Gillies, A. G., Kwak, J., and Fearing, R. S., 2013, "Controllable Particle Adhesion with a Magnetically Actuated Synthetic Gecko Adhesive," *Advanced Functional Materials*, 23(26), pp. 3256-3261.
- [49] Northen, M. T., Greiner, C., Arzt, E., and Turner, K. L., 2008, "A Gecko - Inspired Reversible Adhesive," *Advanced Materials*, 20(20), pp. 3905-3909.
- [50] Ye, Z., Lum, G. Z., Song, S., Rich, S., and Sitti, M., 2016, "Phase Change of Gallium Enables Highly Reversible and Switchable Adhesion," *Advanced Materials*, 28(25), pp. 5088-5092.
- [51] Wang, Y., Tian, H., Shao, J., Sameoto, D., Li, X., Wang, L., Hu, H., Ding, Y., and Lu, B., 2016, "Switchable Dry Adhesion with Step-like Micropillars and Controllable Interfacial Contact," *ACS applied materials & interfaces*, 8(15), pp. 10029-10037.
- [52] Seo, J., Eisenhaure, J., and Kim, S., 2016, "Micro-wedge array surface of a shape memory polymer as a reversible dry adhesive," *Extreme Mechanics Letters*, 9, pp. 207-214.
- [53] Jeong, H. E., Kwak, M. K., and Suh, K. Y., 2010, "Stretchable, adhesion-tunable dry adhesive by surface wrinkling," *Langmuir*, 26(4), pp. 2223-2226.
- [54] Minsky, H., and Turner, K., 2015, "Achieving enhanced and tunable adhesion via composite posts," *Applied Physics Letters*, 106(20), p. 201604.
- [55] Shan, W., and Turner, K., 2017, "Methods for Fast and Reversible Dry Adhesion Tuning between Composite Structures and Substrates.."
- [56] Krueger, R., 2004, "Virtual crack closure technique: history, approach, and applications," *Applied Mechanics Reviews*, 57(2), pp. 109-143.
- [57] Zehnder, A., 2012, "Fracture Mechanics (Lecture Notes in Applied and Computational Mechanics)," Springer, London.
- [58] Je, J., and Lee, J., 2014, "Design, fabrication, and characterization of liquid metal microheaters," *Journal of Microelectromechanical Systems*, 23(5), pp. 1156-1163.
- [59] Schubert, B. E., and Floreano, D., 2013, "Variable stiffness material based on rigid low-melting-point-alloy microstructures embedded in soft poly (dimethylsiloxane)(PDMS)," *Rsc Advances*, 3(46), pp. 24671-24679.
- [60] Siegel, A. C., Bruzewicz, D. A., Weibel, D. B., and Whitesides, G. M., 2007, "Microsolidics: fabrication of three - dimensional metallic microstructures in poly (dimethylsiloxane)," *Advanced Materials*, 19(5), pp. 727-733.
- [61] Haubert, K., Drier, T., and Beebe, D., 2006, "PDMS bonding by means of a portable, low-cost corona system."
- [62] Mark, A. E., M. A. J., B. K. G., 2008, "Determining the optimal PDMS-PDMS bonding technique for microfluidic devices," *Journal of Micromechanics and Microengineering*, 18(6), p. 067001.